

Towards Real-World Indoor Smart Electromagnetic Environments - A Large-Scale Experimental Demonstration

A. Benoni,⁽¹⁾ F. Capra,⁽¹⁾ M. Salucci,⁽¹⁾ *Senior Member, IEEE*, and A. Massa,⁽¹⁾⁽²⁾⁽³⁾⁽⁴⁾ *Fellow, IEEE*

⁽¹⁾ *ELEDIA Research Center (ELEDIA@UniTN - University of Trento)*

DICAM - Department of Civil, Environmental, and Mechanical Engineering

Via Mesiano 77, 38123 Trento - Italy

E-mail: {*arianna.benoni, federico.capra, marco.salucci, andrea.massa*}@unitn.it

Website: www.eledia.org/eledia-unitn

⁽²⁾ *ELEDIA Research Center (ELEDIA@UESTC - UESTC)*

School of Electronic Science and Engineering, Chengdu 611731 - China

E-mail: *andrea.massa@uestc.edu.cn*

Website: www.eledia.org/eledia-uestc

⁽³⁾ *ELEDIA Research Center (ELEDIA@TSINGHUA - Tsinghua University)*

30 Shuangqing Rd, 100084 Haidian, Beijing - China

E-mail: *andrea.massa@tsinghua.edu.cn*

Website: www.eledia.org/eledia-tsinghua

⁽⁴⁾ *School of Electrical Engineering*

Tel Aviv University, Tel Aviv 69978 - Israel

E-mail: *andrea.massa@eng.tau.ac.il*

Website: <https://engineering.tau.ac.il/>

This work has been submitted to the IEEE for possible publication. Copyright may be transferred without notice, after which this version may no longer be accessible.

Towards Real-World Indoor Smart Electromagnetic Environments - A Large-Scale Experimental Demonstration

A. Benoni, F. Capra, M. Salucci, and A. Massa

Abstract

To the best of the authors' knowledge, this work presents the first large-scale indoor experimental assessment of an implementation of the emerging *Smart ElectroMagnetic Environment (SEME)* paradigm, which is based on the deployment of static-passive *EM skins (SP-EMSs)* to enhance the coverage in a 5 [GHz] *Wi-Fi* network. Unlike standard (laboratory-based) validations reported in the state-of-the-art (*SoA*) literature, the scenario at hand mimics a realistic indoor environment to replicate as close as possible the user experience when using commodity devices. Representative results from the experimental field trials are reported to confirm the performance predictions arising from the numerical studies and the tolerance analyses carried out with a commercial ray-tracing (*RT*) tool. Besides experimentally validating the *SEME* idea, this study is also aimed at (roughly) quantifying the economic advantage of a *SEME* implementation, relying on simple-manufacturing/low-cost field manipulating devices without any additional biasing circuitry, with respect to standard approaches that imply the densification of the active radiating sources.

Key words: Smart ElectroMagnetic Environment (*SEME*), Indoor, *Wi-Fi*, Static and Passive *EM Skins (SP-EMSs)*, Ray Tracing (*RT*), Experimental Assessment.

1 Introduction

Recently, there has been an exponential growth of research efforts, from both academy and industry, to develop innovative concepts and cutting-edge technologies for fulfilling the ever-increasing demand for connectivity of current *5G* and future *6G* wireless systems [1]-[5]. Indeed, next generations wireless networks will have to be efficient and smart enough to realize the vision of a fully connected world where the *Internet-of-Everything* (or more the *Internet-of-Emotions*) will ensure seamless and ubiquitous connectivity at an unprecedented scale [6][7]. Towards this end, ultra-massive multiple-input multiple-output (*UM-MIMO*) [8], artificial intelligence [9], orbital angular momentum multiplexing [10], visible-light communications [11], quantum computing [12], and the extension to the terahertz spectrum [3][13] are currently investigated as promising technological recipes for efficiently and reliably building future wireless systems [14]. Moreover, traditional wireless infrastructures are currently undergoing a deep revolution driven by the recent introduction of the so-called *Smart ElectroMagnetic Environment (SEME)* paradigm [15]-[22]. While the propagation environment has been traditionally perceived as an impairment to the propagation of *EM* waves, several *SEME* proofs-of-concept have shown the possibility to control (also doing programmable) its *EM* fingerprint, thus bringing unprecedented new opportunities for enhancing the performance of the whole wireless system not-only acting on the active transmitting/receiving devices [15]-[18].

Innovative *EM* wave manipulating devices such as static-passive electromagnetic skins (*SP-EMSs*) [23]-[28] or reconfigurable-passive *EMSs* (*RP-EMSs*), also referred to as Reconfigurable Intelligent Surfaces (*RISs*) [6][7][11][16][20][29]-[34], have been introduced as cost-effective alternatives to conventional recipes (e.g., increasing the transmit power and deploying additional network infrastructure such as relays [35]) for fulfilling challenging user-experience (*UE*) requirements, while counteracting undesired phenomena such as non-line-of-sight (*NLOS*), fading, and shadowing.

The use of *EMSs* to yield an adequate wireless coverage and to improve the quality-of-service (*QoS*) has been investigated in several indoor [6][7][36]-[38] and outdoor [23][28][33][39]-[41] rich-scattering scenarios hosting wireless communication systems working in either the sub-6GHz [6][23][28] or the millimeter-wave [18][27][35] frequency bands. In a nutshell, *EMSs*

are artificially-engineered surfaces [17][42] consisting of periodic/apperiodic arrangements of specifically-designed sub-wavelength-sized unit cells (*UCs*). The micro-scale descriptors of the *EMSs* can be locally tuned to manipulate the reflection of the impinging *EM* waves so that, at macro-scale, it is possible to afford anomalous reflections towards non-Snell angular directions as well as to generate focused beams [27][28] or contoured footprints [25][26] complying with specific application-driven requirements.

On the one hand, *RP-EMSs* have drawn particular interest thanks to the reconfigurability feature enabled by the presence of tunable components realized with varactor diodes [6], liquid crystals [11], graphene [13], or positive-intrinsic-negative (*PIN*) diode switches [37]. However, *RP-EMSs* have also some cons compared to their “simpler” static implementation (i.e., *SP-EMSs*) such as, for instance, the finite set of discrete states (i.e., 2^N states with an N -bits design [40]) that implies a reduction of the beam-forming capabilities and, often, the generation of spurious beams (e.g., 1-bit structures [37]). Certainly, the number of discrete states of a *UC* can be increased by employing, for instance, more *PIN* diodes or interfacing the varactor diodes with digital to analog converters, but all these countermeasures cause a greater current consumption and they need more expensive/complex control networks [37]. Moreover, the higher architectural complexity of *RP-EMSs* turns out in a stronger dependence on the manufacturing tolerances as well as on the non-ideal characteristics of the embedded tunable loads. This may cause significant deviations from the nominal/simulated behavior [40].

Regardless of static or reconfigurable behaviour, the prototyping of *EMS*-aided wireless communications and real-world field trials are still scarce and more tests are necessary towards an industrial perspective [39][40][41]. Currently, relatively few measurement campaigns have been documented in the *SoA* literature to prove that the placement of an *EMS* onto a building wall could be a cost-effective solution to circumvent coverage blockages [37].

To the best of the authors’ knowledge, while accurate physics-driven path loss models, which overcome traditional “simplistic” mathematical *EM* predictions, have been validated with dedicated experimental measurements [14][35] and the potentialities of *RIS*-assisted wireless communications have been experimentally assessed in both outdoor [39]-[40] and indoor [6][7][36]-[38] scenarios, a more exhaustive set of field trials is still needed to enable the transition from

pre-commercial prototypes to an effective commercial deployment of a *EMS*-based *SEME* [39]. As a matter of fact, most of the test-beds described in the literature are still quite far from a real-world every-day-life context since *ad-hoc* measurement setups are generally considered. More specifically, the focus is usually on the optimization of a single *TX-RX* link in artificially-generated *NLOS* conditions [6][7][36] where the *EMS* is mounted on a tripod or equivalent support [41], while highly-directive and properly-oriented antennas (e.g., horns [40][41]) are used to illuminate and/or to collect the reflected *EM* signal. Furthermore, experimental validations have been generally limited to mono-chromatic signals [40] and there are not documented large-scale experiments on the exploitation of *SP-EMSs* in real-world *SEMEs*. Indeed, currently available works are exclusively dedicated to the exploitation of more complex/expensive 1-bit [39][40][43][44] or multi-bit [7][37][38] *RP-EMSs*.

This paper presents the outcomes of a large-scale experimental demonstration of a real-world indoor *SEME* enabled by *SP-EMSs*. The main and innovative contributions of this work over the existing literature consist in (i) the first, to the best of the authors' knowledge, experimental deployment of cost-effective *SP-EMSs* to improve the indoor coverage in a pre-existing 5 [GHz] *Wi-Fi* network, (ii) an in-depth modeling of the *EM* propagation in complex *EMS*-added indoor environments to numerically predict the dependence of the *EM* coverage on the key descriptors of the *SP-EMS* (e.g., *EMS* aperture size and post-manufacturing positioning), (iii) a comparative evaluation of the *Total Cost of Ownership (TCO)* [46] for a wireless network using *SP-EMSs* along with the analysis of the *QoS* and *UE* indexes to give the readers a complete picture of the system performance, not only limited to physical-layer parameters.

The outline of the paper is as follows. Section 2 describes the indoor large-scale test-bed by reporting the results of its numerical and experimental characterization, as well. The implementation of a *SP-EMSs*-based *SEME* scheme is then detailed, discussed, and also experimentally-validated in Sect. 3 where its pros/cons from an economic point of view are also analyzed. Eventually, some final remarks and conclusions are drawn (Sect. 4).

2 Test-Bed - Reference Scenario

The experimental test bed is the *Mesiano* building of the Department of Civil, Environmental, and Mechanical Engineering (*DICAM*) of the University of Trento, in Trento, Italy (Fig. 1). The building was a former sanatorium around 1920 and it has been successively converted to the Engineering Faculty in 1984. It is composed by five floors covering a total area of approximately 13×10^3 [m²]. *Wi-Fi* connectivity is provided by means of *Aruba AP-304* access points (*APs*) operating in the 5 [GHz] band with a maximum transmit power of $P_{TX} = 23$ [dBm] [50]. As a representative example, the following discussion will be focused on the second floor, which includes five wide hallways (labeled as “*A*”, “*B*”, “*C*”, “*D*”, and “*E*”), alongside several offices, teaching rooms, and two stairwells and elevators to access the other floors [Fig. 2(a)].

2.1 EM Modeling

To have a reliable prediction of the existing *Wi-Fi* coverage, the commercial *RT*-based simulator Altair WinProp [45] has been used to estimate the received power distribution on the layer at a constant height of $h = 1.2$ [m] that mimics the typical area where the hand-held smartphone of a standing person is located (Fig. 3). Towards this end, an accurate *EM* model of the scenario at hand has been created in the simulation suite starting from high-fidelity *CAD* drawings that include the exact location of each structural element (i.e., walls, windows, and doors) as well as of the actually deployed *APs*. The *EM* behavior of the *APs* has been modeled by importing, in the setup of the radiating sources of the *RT* model, the full-wave simulated pattern of the monopole antenna indicated in the manufacturer data-sheet [50].

Figure 2(a) shows the *RT*-simulated absolute map of the received power, P_{RX} , at the carrier frequency of $f = 5.64$ [GHz] (i.e., *IEEE 802.11* channel $\xi = 128$) on a grid of sampling points uniformly spaced by $\delta_x = \delta_y = 0.25$ [m] where the position $\mathbf{r}_\Psi = (x_\Psi, y_\Psi, z_\Psi)$ of each *AP* (i.e., Ψ_γ , $\gamma \in \{A, B, C, D, E\}$) serving the area under test is indicated, as well. As it can be inferred, the most critical regions in terms of *Wi-Fi* coverage are the two 27 [m] long hallways “*A*” and “*B*”, located in the bottom part of the map, having an extension of $\Lambda(A) = \Lambda(B) = 67.5$ [m²] as well as, albeit to a lesser extent, the central hallway “*C*” $\Lambda(C) = 60.5$ [m²] wide. This is not surprising, since the corresponding *APs* (i.e., Ψ_A , Ψ_B , and

Ψ_C) are located *beyond* the extreme left/right/left walls of the related hallways.

To give some insights on the experienced *QoS* of a user, let us analyze more in detail the distribution of the received power predicted in the hallway “A” area [Fig. 4(a)] by noticing that the same outcomes can be drawn for “B” since both zones share almost the same $P_{RX}(x, y)$ distribution because of their geometric/*EM* symmetry [Fig. 2(a)].

By setting the threshold value to $P_{th} = -65$ [dBm] for a strong *Wi-Fi* connection and suitable data-transfer rates for services such as video streaming and voice-over-*IP* (*VoIP*) [28][51], one can obtain the binary map in Fig. 4(b) where the power level turns out to be below the target one within the region-of-interest (*RoI*) Ω_A . This latter extends on a non-negligible area of $\Lambda_{Ref}(\Omega_A) = 23.13$ [m²] ($\rightarrow \Delta\Lambda_{Ref}^A \approx 34$ % being $\Delta\Lambda^\gamma \triangleq \frac{\Lambda(\Omega_\gamma)}{\Lambda(\gamma)}$) and it is located in the right portion of the hallway, that is, in the opposite direction to the *AP* Ψ_A , which is installed beyond the left wall in $\mathbf{r}_{\Psi_A} = (2.00, 2.48, 2.88)$ [m] (Fig. 4).

For completeness, the thresholded map of the second floor is shown in Fig. 5(a) where $\Lambda_{Ref}(\Omega_B) = 21.88$ [m²] ($\rightarrow \Delta\Lambda_{Ref}^B \approx 33$ %) and $\Lambda_{Ref}(\Omega_C) = 0.8$ [m²] ($\rightarrow \Delta\Lambda_{Ref}^C \approx 1.5$ %), while there is an optimal coverage in the remaining areas under test (i.e., “D” and “E” hallways).

2.2 Experimental Assessment

Before proceeding to the manufacturing and the deployment of the *EMSs* to enhance the *Wi-Fi* coverage in the *RoIs*, a measurement campaign has been carried out to further assess the simulation outcomes. To faithfully emulate the *UE* in the existing *Wi-Fi* network, the measurement tests have been performed by avoiding directional antennas (e.g., horns) connected to high-end instrumentations mounted on moving supports as in the *SoA* literature (e.g., [40][41]) since it could result in an optimistic over-estimation of the *QoS* perceived by the actual users. Otherwise, the map of the received power has been realized by collecting the data with an hand-held Android smartphone [Fig. 6(b)] and setting the measurement locations, marked on the floor with paper scotch tape [Fig. 6(a)], to the sampling points of the *RT* solver. To filter out outliers and the measurement noise, the received power measured at each probing location has been averaged over a time window of $\Delta t = 10$ [sec].

Regardless of several (intentional) non-idealities of the adopted probing setup, the overall mea-

sured coverage map of the entire floor turns out quite close to the simulated one [Fig. 2(b) vs. Fig. 2(a)].

For instance, let us compare the measured P_{RX} map in the hallway “A” [Fig. 7(a)] with the simulated one in Fig. 4(a). Besides the good matching of the distribution of the received power, which decreases with the distance from the AP, it is worth noting that the existence of the low-coverage *RoI* Ω_A is confirmed in the measured (thresholded) map [Fig. 7(b)] and, even more, that the extension of this latter (i.e., $\tilde{\Lambda}_{Ref}(\Omega_A) = 20.13 \text{ [m}^2\text{]}$) turns out to be close to the *RT*-predicted one $\Lambda_{Ref}(\Omega_A)$ [Fig. 4(b)].

For completeness, Figure 5(b) shows the measured version of the thresholded coverage map where one can infer that $\tilde{\Lambda}_{Ref}(\Omega_B) = 23.93 \text{ [m}^2\text{]}$ [i.e., $\tilde{\Lambda}_{Ref}(\Omega_B) \approx \Lambda_{Ref}(\Omega_B)$] and $\tilde{\Lambda}_{Ref}(\Omega_C) = 0.8 \text{ [m}^2\text{]}$ [i.e., $\tilde{\Lambda}_{Ref}(\Omega_C) \approx \Lambda_{Ref}(\Omega_C)$] as further check of the *RT*-prediction.

3 SEME Test-Bed

Once the presence of low-coverage *RoIs* in the “reference scenario” has been detected, an *EMS*-based implementation of the *SEME* paradigm consists in the selection of the most suitable *EMS*s design (Sect. 3.1) by also predicting their effects (Sect. 3.2) and estimating possible performance degradations caused by the (almost unavoidable) tolerances in both the manufactured prototypes and their final real-world deployment (Sects. 3.3-3.4). Towards a commercial deployment, an analysis from the economic viewpoint (Sect. 3.5) is also necessary.

3.1 SP-EMS Design

Figure 8 provides a 3-D geometrical sketch of the *SEME* configuration used to improve the *Wi-Fi* coverage within the hallway “A”. The position and the extension of the *SP-EMS* have been chosen to comply with both *EM* requirements and architectural constraints by considering, as a realistic strategy, that the existing *Wi-Fi* infrastructure cannot be modified. More specifically, the following criteria have been adopted: (i) the reflective aperture of the *EMS*, S_A , should harvest as much as possible *EM* energy from the AP Ψ_A ; (ii) the *SP-EMS* must be mounted on the available wall surface without altering the building rules in terms of security and maintenance.

By denoting with $\mathbf{r}_S = (x_S, y_S, z_S)$ and $\mathbf{r}_\Omega = (x_\Omega, y_\Omega, z_\Omega = h)$ the barycenter of the *SP-EMS* and the desired (anomalous) focusing point belonging to the spatial region Ω at height h where the received power [49]

$$P_{RX}(\mathbf{r}) = \frac{\lambda^2 G_{RX}}{8\pi\eta} |\mathcal{E}(\mathbf{r})|^2 \quad (1)$$

is insufficient for guaranteeing a given *QoS* (i.e., $P_{RX}(\mathbf{r}) < P_{th}$, $\mathbf{r} \in \Omega$, P_{th} being the desired coverage threshold), respectively, the *SP-EMS* has been positioned on the wall just in front of the *AP*, at the location $\mathbf{r}_{S_A} = (0.15, 2.69, 2.45)$ [m] [Fig. 8(b)], to ensure *LOS* conditions with both \mathbf{r}_{Ψ_A} and \mathbf{r}_{Ω_A} ($\mathbf{r}_{\Omega_A} = (17.5, 2.33, 1.20)$ [m] - Fig. 7), but also avoiding to overlap (even partially) the doors present in the same site.

The *SP-EMS* has been then designed starting from the computation of the incidence, (θ_i, φ_i) , and the reflection, (θ_r, φ_r) , angular directions (Fig. 3)

$$\begin{cases} (\theta_i, \varphi_i) = \mathcal{F}\{\mathbf{r}_\Psi, \mathbf{r}_S\} \\ (\theta_r, \varphi_r) = \mathcal{F}\{\mathbf{r}_\Omega, \mathbf{r}_S\} \end{cases}, \quad (2)$$

$\mathcal{F}\{\cdot\}$ being the Cartesian-to-spherical operator mapping either \mathbf{r}_Ψ or \mathbf{r}_Ω to the corresponding elevation and azimuth angles in the local coordinate system $\mathbf{r}' = (x', y', z')$ centered in \mathbf{r}_S (Fig. 9) [28]. In (1), λ ($\lambda \triangleq \frac{c_0}{f}$) and η ($\eta \triangleq \sqrt{\frac{\mu_0}{\epsilon_0}}$) are the wavelength at the working frequency f and the impedance of the free-space with permittivity ϵ_0 and permeability μ_0 , respectively, c_0 ($c_0 \triangleq \frac{1}{\sqrt{\epsilon_0\mu_0}}$) being the speed of light, while G_{RX} is the maximum gain of the receiver and $\mathcal{E}(\mathbf{r})$ is the electric field.

According to (2), the values of the incidence and reflection angles turn out to be equal to $(\theta_i^A, \varphi_i^A) = (14.5, 116.0)$ [deg] and $(\theta_r^A, \varphi_r^A) = (4.29, -106.1)$ [deg], by also numerically confirming the need for a double-anomalous (i.e., non-Snell in both elevation and azimuth) reflection to reach the *RoI*.

Figure 9 shows the reference monolithic layout adopted for synthesizing the *SP-EMSs* of the *SEME* test-bed. The *EMS* aperture \mathcal{S} of side L consists of a set of $N \times N$ metal-backed *UCs* arranged in a uniform square lattice with half-wavelength inter-element spacing $\ell_{UC} = \frac{\lambda}{2}$ [$L = (N \times \ell_{UC})$]. More specifically, the dual-layer stacked structure in [47] has been chosen as

the *EMS* atom to excite a multi-resonant behavior and to yield a smooth phase variation in a sufficiently wide angular range by using relatively inexpensive dielectric materials and off-the-shelf thicknesses. To further keep the design and the manufacturing complexity as low as possible, the bottom layer and the top one of each *UC* have been realized by using identical *FR-4* substrates of relative permittivity $\varepsilon_r = 4.4$, loss tangent $\tan \delta = 0.02$, and thickness $t = 1.6$ [mm] [Fig. 9(a)], while two square metallic patches of side ℓ_1 and $\ell_2 = (\alpha \times \ell_1)$, $\alpha = 0.8$ being a scaling factor [47], have been etched on the top face of each printed circuit board (*PCB*) layer to enable a local fine-tuning of the reflection phase.

The skin size L has been chosen as the best trade-off between the capability of collecting/re-radiating a sufficient amount of *EM* energy and the overall cost as well as its physical encumbrance, which should be kept as low as possible to minimize both the economic and the architectural impact of the *SEME* solution. Towards this end, the relationship between the *EMS* dimension and the achievable coverage enhancement has been analyzed.

With reference to the hallway “A”, as a representative example, L_A has been varied within the range $L_A \in [0.28, 0.80]$ [m] (i.e., $N_A \in [10, 30]$) and for each *EMS* aperture (i.e., the number of *UCs* per side, N_A), the two-step synthesis method detailed in [25] has been applied to derive the set of $N \times N$ geometric degrees-of-freedom, $\underline{\chi} = \{\ell_1^{mn}; m, n = 1, \dots, N\}$, that model the metallic pattern of the corresponding *EMS* layout. Figure 10(a) summarizes the outcomes of such an analysis by showing the behavior of the cumulative density function (*CDF*) of the received power inside the hallway at hand

$$\Theta \left\{ P_{RX}(\mathbf{r}) | \hat{P} \right\} = \Pr \left\{ P_{RX}(\mathbf{r}) \leq \hat{P} \right\} \quad (3)$$

where $\Pr \{ \cdot \}$ denotes the probability function and $\hat{P} \in [-75, -40]$ [dBm]. As it can be inferred, there is always a non-negligible improvement of the wireless coverage with respect to the “reference” scenario and, as expected, wider *EMS* apertures correspond to more significant enhancements. Quantitatively, the probability of being below the threshold ($\Theta_{th} = \Theta \{ P_{RX}(\mathbf{r}) | P_{th} \}$) progressively decreases from $\Theta_{th}^{Ref} = 45$ % down to $\Theta_{th}^{SEME}(A) = 12$ % for the widest *EMS* aperture (i.e., $L_A = 0.8$ [m]), $\Theta_{th}^{SEME}(A) = 35$ % being the probability for the smallest skin ($L_A = 0.28$ [m] $\rightarrow N_A = 10$).

A similar trend holds true for the reduction of the *RoI* area, ρ_{SEME} , defined as

$$\rho_{SEME}(\Omega) \triangleq \frac{\Lambda_{Ref}(\Omega) - \Lambda_{SEME}(\Omega|L)}{\Lambda_{Ref}(\Omega)}, \quad (4)$$

whose behavior versus the *EMS* size L and the corresponding values are reported in Fig. 10(b) and Tab. I, respectively. It turns out that $\rho_{SEME}(\Omega_A) = 37.8\%$ and $\rho_{SEME}(\Omega_A) = 79.5\%$ for the smallest (i.e., $L_A = 0.28$ [m]) and the largest (i.e., $L_A = 0.80$ [m]) *SP-EMS*, respectively.

By taking into account both *EM* coverage requirements and installation constraints, the intermediate-size *EMS* with $L_A = 0.55$ [m] ($N_A = 20$) [Fig. 9(a)] has been selected as the best compromise, since $\Theta_{th}^{SEME}(A) = 18\%$ [Fig. 10(a)] and $\rho_{SEME}(\Omega_A) = 70\%$ [Fig. 10(b)] while wider apertures provide only marginal improvements.

For comparison purposes, the coverage enhancement yielded by installing another *AP* [referred as standard (*STD*) approach] on the opposite side of the hallway ($\mathbf{r}_{\Psi_A^{(2)}} = (29.2, 2.00, 2.88)$ [m]) has been predicted, as well. As expected, the use of an active device allows one to outperform the fully-passive *SEME* solution in terms of coverage enhancement (i.e., $\Theta_{th}^{STD}(A) = 3\%$ [Fig. 10(a)] and $\rho_{STD}(\Omega_A) = 95\%$ [Fig. 10(b)]), but, besides the need of more transmitting power and higher economic costs (see Sect. 3.5), adding one *AP* may not be a feasible solution in many practical situations due to the additional cabling and network infrastructure.

3.2 EM Modeling

A pictorial 3D representation of the *EM* behavior of the *SP-EMS* in Fig. 9(a) is shown in Fig. 11 where the full-wave simulated [48] directivity pattern is reported. As it can be observed, the synthesized *EMS* correctly radiates a pencil beam towards the desired anomalous reflection direction, the (simulated) maximum directivity being equal to $D_{max} = 30.73$ [dB], whose effect is a noticeable increase of the received power within the entire hallway “A” [Fig. 12(a) vs. Fig. 4(a)] as pointed out by the difference map ΔP_{RX} ,

$$\Delta P_{RX}(\mathbf{r}) \triangleq P_{RX}^{SEME}(\mathbf{r}) - P_{RX}^{Ref}(\mathbf{r}), \quad (5)$$

in Fig. 12(c). Quantitatively, it turns out that the average $[\Delta P_{RX}^{\text{avg}}(A) \triangleq \frac{1}{\Lambda(A)} \int_A \Delta P_{RX}(\mathbf{r}) d\mathbf{r}]$ and the maximum $[\Delta P_{RX}^{\text{max}}(A) \triangleq \max_{\mathbf{r} \in A} \{\Delta P_{RX}(\mathbf{r})\}]$ power increment are equal to $\Delta P_{RX}^{\text{avg}}(A) = 2.64$ [dB] and $\Delta P_{RX}^{\text{max}}(A) = 9.60$ [dB], respectively (Tab. I).

From a *UE* perspective, the effect of the *SP-EMS* is pointed out by the thresholded map in Fig. 12(b) where the *RoI* extension reduces down to $\Lambda_{SEME}(\Omega_A) = 6.94$ [m²] ($\rightarrow \Delta\Lambda_{SEME}^A \approx 10$ %) from $\Lambda_{Ref}(\Omega_A) = 23.13$ [m²] in Fig. 4(b) [i.e., $\rho_{SEME}(\Omega_A) = 70$ %].

For completeness, the results of the *EMS*-based *SEME* implementations in the zones “B” and “C” are summarized in Fig. 13 and Fig. 14, respectively, where the corresponding difference maps and *CDF*s are reported.

As expected, the distribution of the ΔP_{RX} values in the hallway “B” is almost symmetrical to that in the hallway “A” [Fig. 13(a) vs. Fig. 12(c)], while the related statistical indexes are very close being $\Delta P_{RX}^{\text{avg}}(B) = 2.52$ [dB] and $\Delta P_{RX}^{\text{max}}(B) = 8.21$ [dB] (Tab. I vs. Tab. II). Similar outcomes can be drawn from the behavior of the *CDF* in Fig. 13(b).

Concerning the “C” hallway, the deployment of the smaller ($L_C = 0.32$ [m]) *SP-EMS* in Fig. 9(b) as in Fig. 15 [$(\theta_i^C, \varphi_i^C) = (15.33, 28.07)$ [deg] and $(\theta_r^C, \varphi_r^C) = (4.19, -43.60)$ [deg]] has been enough to fulfill the *QoS* requirements since $\rho_{SEME}(\Omega_A) = 100$ % being $\Theta_{th}^{SEME}(C) = 0.0$ % [Fig. 14(b)]. Indeed, a lower and limited coverage improvement than that for the scenario “A” (“B”) [Fig. 14(a) vs. Fig. 12(c) and Fig. 13(a)] was required to reach the target threshold of $P_{th} = -65$ [dBm] (e.g., $\Delta P_{RX}^{\text{avg}}(C) = 0.84$ [dB] vs. $\Delta P_{RX}^{\text{avg}}(A) = 2.64$ [dB] and $\Delta P_{RX}^{\text{avg}}(B) = 2.52$ [dB] - Tab. I vs. Tab. II).

3.3 Sensitivity Analysis

Before proceeding to the manufacturing and the installation of the *SP-EMS*s, a sensitivity analysis has been carried out to predict possible performance degradations caused by the (almost unavoidable) tolerances in their final deployment in the real test-bed. Towards this end, a set of positioning inaccuracies has been modeled by considering an error along the horizontal (Δy) and/or the vertical (Δz) axes [Fig. 16(a)].

With reference to the deployment in the hallway “A”, Figure 16(b) plots the values of the *RoI* reduction, $\rho_{SEME}(\Omega_A)$, versus the offsets in the range $(\Delta y, \Delta z) \in [-0.1, 0.1]$ [m]. Despite

the non-negligible change of the incidence/reflection angles that would be necessary for a re-design of the skin when moving its barycenter (e.g., $(\Delta\theta_i^A, \Delta\varphi_i^A) = (-0.75, 17.18)$ [deg] and $(\Delta\theta_r^A, \Delta\varphi_r^A) = (0.41, -2.72)$ [deg] when $\Delta y = \Delta z = 0.1$ [m]), the “nominal” *SP-EMS* proves to be robust to the positioning errors. As a matter of fact, $\rho_{SEME}(\Omega_A) \geq 26.9\%$ whatever the combination of Δy and Δz values [Fig. 16(b)].

These conclusions are further confirmed by the plots of the *CDF* in the presence of either an horizontal [$\Delta z = 0$ [m], $\Delta y \in [-0.1, 0.1]$ [m] - Fig. 16(c)] or a vertical [$\Delta y = 0$ [m], $\Delta z \in [-0.1, 0.1]$ [m] - Fig. 16(d)] shift of the nominal *EMS* barycenter since always $\Theta_{th}^{SEME}(A) \leq \Theta_{th}^{Ref}$ and the maximum deviation from the nominal value is around than 15 % [Figs. 16(c)-16(d)], the main impact being due to the horizontal errors [Fig. 16(d)].

3.4 Experimental Assessment

A prototype of the *SP-EMS* S_A of side $L_A = 0.55$ [m] has been fabricated via *PCB* manufacturing using off-the-shelf *FR-4* substrates [Fig. 17(a)] and, successively, it has been installed in the experimental test-bed as modeled in the numerical analyses [Fig. 17(b) vs. Fig. 8]. Three small removable mechanical supports, made of plywood, fixed to the wall with steel nails (Fig. 17) have been used to easily mount/remove the *SEME* device for performing several field trials.⁽¹⁾ After the *EMS* deployment, the *Wi-Fi* coverage (measured) in the hallway “A” is shown in Fig. 18(a), while the difference map with respect to the (measured) reference distribution of Fig. 7(a) is reported in Fig. 18(b). Such experimental results confirm the outcomes of the numerical assessment since, besides the visible improvement of the received power distribution inside the area under test [Fig. 18(a) vs. Fig. 7(a) and Fig. 18(b)], there is a close agreement also quantitatively. As a matter of fact, the measured value of the average increment of the received power in the complete hallway turns out to be just 0.24 [dB] different from the predicted one (i.e., $\Delta\tilde{P}_{RX}^{avg}(A) = 2.4$ [dB] vs. $\Delta P_{RX}^{avg}(A) = 2.64$ [dB]). Similarly, the maximum measured value has been equal to $\Delta\tilde{P}_{RX}^{max}(A) = 9.0$ [dB], $\Delta P_{RX}^{max}(A) = 9.60$ [dB] being the prediction, while the standard deviation - as expected - more significantly differs (i.e., $\Delta\tilde{P}_{RX}^{dev}(A) = 4.0$

⁽¹⁾From a practical point of view, it is worth mentioning that the prototype is quite lightweight (the total weight being approximately 0.5 [Kg]). Therefore, it is easy to deploy a permanent installation using (for instance) proper glues or specific double sided tapes.

[dB] vs. $\Delta P_{RX}^{\text{dev}}(A) = 2.36$ [dB]) due to the non-idealities and inaccuracies in the measurement process.

As for the *RoI* extension, the experimental tests indicate that it has been reduced down to $\tilde{\Lambda}_{SEME}(\Omega_A) = 5.50$ [m²] with a (measured) coverage improvement of $\tilde{\rho}_{SEME}(A) = 72.7$ %, which is even better than the predicted one [i.e. $\rho_{SEME}(A) = 70$ %]. This implies a probability of being below the threshold smaller than 10 % (i.e., $\tilde{\Theta}_{th}^{SEME}(A) = 8.5\%$ - Fig. 19) starting from $\tilde{\Theta}_{th}^{Ref}(A) = 30$ %, while the prediction was more conservative since $\Theta_{th}^{SEME} = 18$ % [Fig. 10(a)] being $\Theta_{th}^{Ref} = 45$ %.

Besides the experimental assessment at the “physical” layer with the measurements of the received power, the effectiveness of the *SEME* implementation has been also validated from the *UE* viewpoint. Towards this end, the OOKLA Speedtest[®] benchmark [52] has been run on a laptop connected to the *AP* Ψ_A to evaluate the impact of the *SP-EMS* \mathcal{S}_A on the achievable speed in the download and the upload links. Figure 20 shows the screenshots of such tests at the instant in which the maximum throughput has been recorded. The *SEME* implementation enables a remarkable improvement in both the download [$\mathcal{D}_{Ref}^{\text{max}}(A) = 110.12$ [Mbps] vs. $\mathcal{D}_{SEME}^{\text{max}}(A) = 131.16$ [Mbps] - Fig. 20(a) vs. Fig. 20(c)] and the upload [$\mathcal{U}_{Ref}^{\text{max}}(A) = 84.49$ [Mbps] vs. $\mathcal{U}_{SEME}^{\text{max}}(A) = 108.19$ [Mbps] - Fig. 20(b) vs. Fig. 20(d)] links, respectively.

For completeness, Table III gives the measured statistics (minimum, maximum, average, and standard deviation) of both download/upload throughput (\mathcal{D}/\mathcal{U}) and latency ($\mathcal{L}_D/\mathcal{L}_U$). As it can be noticed, the average download throughput significantly increases being $\Xi_D(A) = 33.6$ %, while the average latency of the download link is more than halved (i.e., $\Xi_{\mathcal{L}_D}(A) = -57.6$ %) [$\Xi_{\zeta}(\gamma) \triangleq \frac{\zeta_{SEME}^{\text{avg}}(\gamma) - \zeta_{Ref}^{\text{avg}}(\gamma)}{\zeta_{Ref}^{\text{avg}}(\gamma)}$, $\zeta \in \{\mathcal{D}, \mathcal{L}_D, \mathcal{T}_D, \mathcal{U}, \mathcal{L}_U\}$]. For instance, this means that the time required to download a 7 [GB] 4K-definition movie in the reference scenario would be $\mathcal{T}_D^{Ref}(A) = 9.74$ [min], while it would reduce to $\mathcal{T}_D^{SEME}(A) = 7.29$ [min] in the *SEME* scenario at hand with a time saving of $\Xi_{\mathcal{T}_D}(A) = 25.2$ %.

Similar conclusions hold true in upload, the throughput and the latency being $\Xi_U(A) = 19.1\%$ and $\Xi_{\mathcal{L}_U}(A) = -52.9\%$ better than in the reference scenario (Tab. III).

3.5 Total Cost of Ownership (TCO) Analysis

In order to envisage a commercial deployment of the proposed *SEME* implementation, a comprehensive evaluation of the pros/cons also from an economic point of view is necessary also besides the numerical/experimental assessment of its *EM* performance. Towards this end, a preliminary estimation of the *Total Cost of Ownership (TCO)* [46] has been performed.

The *TCO*, \mathbb{C} , is an index commonly adopted to estimate the long-term budget for the implementation of a technological solution for making informed decisions about the investments plan. As a matter of fact, it allows one to have a feeling on the economic effectiveness and the sustainability of a new hardware purchase/deployment devoted to improve the *Wi-Fi* network performance. More specifically, the *TCO* accounts for different terms related to (i) the purchasing (“cost of acquisition”, \mathcal{C}_a), the installation (“cost of commissioning”, \mathcal{C}_c), the power consumption (“cost of operation”, \mathcal{C}_o), and the removal at the end of the life-cycle (“cost of decommissioning”, \mathcal{C}_d) of a device [46]

$$\mathbb{C} = \mathcal{C}_a + \mathcal{C}_c + \mathcal{C}_o + \mathcal{C}_d. \quad (6)$$

Let us consider the hallway “A” as a representative test case of a class of common spaces in public buildings. The *PCB* manufacturing of the *SP-EMS* \mathcal{S}_A had a cost of $\mathcal{C}_a^{SEME}(A) = 100$ [\$] (Tab. IV),⁽²⁾ while the panel installation had an almost negligible impact on the overall expense (i.e., $\mathcal{C}_c^{SEME}(A) = 5$ [\$] - Tab. IV). Unlike *RP-EMS*s deployments [41], there are no recurrent costs for the electric energy consumption ($\mathcal{C}_o^{SEME}(A) = 0$ [\$/year] - Tab. IV) thanks to the absence of any biasing circuits. Moreover, the final decommissioning implies no additional costs since there is no cabling to remove nor change to the *Wi-Fi* network infrastructure (i.e., $\mathcal{C}_d^{SEME}(A) = 0$ [\$] - Tab. IV). It turns out that the *TCO* for such a *SEME* implementation is equal to $\mathbb{C}_{SEME}(A) = 105$ [\$] independently on the duration of its life-cycle.

Differently, a *STD* approach based on the deployment of an additional (second) *AP*, although more effective in terms of *EM* radiation (Fig. 10), would imply higher costs. Approximately, the purchasing, the installation, and the final removal of another *AP* would need $\mathcal{C}_a^{STD}(A) + \mathcal{C}_c^{STD}(A) + \mathcal{C}_d^{STD}(A) = 1100$ [\$], while the annual cost for the power consumption would

⁽²⁾Due to the very simple *SP-EMS* layout [Fig. 9(a)] and the exploitation of rather inexpensive dielectric boards, manufacturing costs are expected to be remarkably lower in a large-scale commercial production, while here the sample was a prototype realized with a dedicated production.

amount to $C_o^{STD}(A) = 50$ [\$/year] (Tab. IV).

Consequently, the foreseen overall economic advantage of the *SEME* solution at hand over the *STD* one in a time window of $\Delta t = 5$ [years] (i.e., a medium-long term) would be equal to $\Delta C(A|\Delta t)|_{\Delta t=5[\text{years}]} = 1245$ [\$] [$\Delta C(A|\Delta t) \triangleq C_{STD}(A|\Delta t) - C_{SEME}(A)$] that is of about $\Xi_C(A|\Delta t)|_{\Delta t=5[\text{years}]} \approx 92\%$ [$\Xi_C(A|\Delta t) \triangleq \frac{C_{STD}(A|\Delta t) - C_{SEME}(A)}{C_{STD}(A|\Delta t)}$]. Even more interestingly, it turns out that the average cost saving would be of about $\frac{\Delta C(A|\Delta t)|_{\Delta t=5[\text{years}]}}{\Lambda(A)} \approx 18.4$ [\$/m²]. This latter outcome clearly points out the great potential of such a *SEME* implementation from a practical perspective.

4 Conclusions

In this work, the first - to the best of the authors' knowledge - large-scale indoor experimental assessment of an implementation of the emerging *SEME* paradigm, which is based on the deployment of *SP-EMSs* realized with low-cost off-the-shelf *PCB* substrates and not requiring any biasing circuitry, has been documented. A measurement campaign, aimed at replicating as much as possible a real-life *UE* by using commodity devices and adopting non-ideal probing conditions, has been carried out to confirm the performance predictions drawn from an extensive numerical/tolerance analysis. The results from both the numerical and the experimental assessments have proved the following main outcomes:

- *SP-EMSs* are suitable devices for enhancing the coverage of large rich-scattering indoor areas without any modification to the existing *Wi-Fi* network infrastructure, thus enabling a seamless integration with the existing *APs* and, more in general, within the network architecture as well as the buildings;
- preliminary *RT*-based numerical studies are reliable assets for faithfully predicting the performance of *SP-EMSs*-based *SEME* implementations in order to identify the most suitable layouts/deployments for a successive prototyping/installation;
- the synthesized *SP-EMSs* exhibit a good robustness to the positioning errors that potentially occur in real-world deployments;

- the proposed *SEME* implementation turns out to be economically advantageous over a traditional (active) coverage-enhancement strategies.

Future works will be aimed at implementing commercially-ready *SEMEs* and at developing computationally-efficient strategies for their artificial intelligence-driven prototyping [26] and optimal planning [23][28] towards a mass-market and a huge real-world commercial deployment.

Acknowledgements

This work benefited from the networking activities carried out within the Project "MITIGO - Mitigazione dei rischi naturali per la sicurezza e la mobilita' nelle aree montane del Mezzogiorno" (Grant no. ARS01_00964) funded by the Italian Ministry of Education, University, and Research within the PON R&I 2014-2020 Program (CUP: B64I20000450005) and the Project "SPEED" (Grant No. 6721001) funded by National Science Foundation of China under the Chang-Jiang Visiting Professorship Program. A. Massa wishes to thank E. Vico for her never-ending inspiration, support, guidance, and help.

References

- [1] H. Tataria, M. Shafi, A. F. Molisch, M. Dohler, H. Sjoland, and F. Tufvesson, "6G wireless systems: Vision, requirements, challenges, insights, and opportunities," *Proc. IEEE*, vol. 109, no. 7, pp. 1166-1199, Jul. 2021.
- [2] M. Noor-A-Rahim, Z. Liu, H. Lee, M. O. Khyam, J. He, D. Pesch, K. Moessner, W. Saad, and H. V. Poor, "6G for Vehicle-to-Everything (V2X) communications: Enabling technologies, challenges, and opportunities," *Proc. IEEE*, vol. 110, no. 6, pp. 712-734, Jun. 2022.
- [3] Y. J. Guo, M. Ansari, R. W. Ziolkowski, and N. J. G. Fonseca, "Quasi-optical multi-beam antenna technologies for B5G and 6G mmWave and THz networks: A review," *IEEE Open J. Antennas Propag.*, vol. 2, pp. 807-830, 2021.

- [4] M. Giordani, M. Polese, M. Mezzavilla, S. Rangan and M. Zorzi, "Toward 6G networks: Use cases and technologies," *IEEE Commun. Mag.*, vol. 58, no. 3, pp. 55-61, Mar. 2020.
- [5] C. Huang, S. Hu, G. C. Alexandropoulos, A. Zappone, C. Yuen, R. Zhang, M. Di Renzo, and M. Debbah, "Holographic MIMO surfaces for 6G wireless networks: Opportunities, challenges, and trends," *IEEE Trans. Wireless Commun.*, vol. 27, no. 5, pp. 118-125, Oct. 2020.
- [6] A. Araghi, M. Khalily, M. Safaei, A. Bagheri, V. Singh, F. Wang, and R. Tafazolli, "Re-configurable intelligent surface (RIS) in the sub-6 GHz band: Design, implementation, and real-world demonstration," *IEEE Access*, vol. 10, pp. 2646-2655, Jan. 2022.
- [7] S. Kayraklik, I. Yildirim, Y. Gevez, E. Basar, and A. Gorcin, "Indoor coverage enhancement for RIS-assisted communication systems: Practical measurements and efficient grouping," 2022, arXiv:2211.07188 [eess.SP].
- [8] Y. Zheng, C.-X. Wang, R. Yang, L. Yu, F. Lai, J. Huang, R. Feng, C. Wang, C. Li, and Z. Zhong, "Ultra-massive MIMO channel measurements at 5.3 GHz and a general 6G channel model," *IEEE Trans. Veh. Technol.*, vol. 72, no. 1, pp. 20-34, Jan. 2023.
- [9] K. B. Letaief, Y. Shi, J. Lu, and J. Lu, "Edge artificial intelligence for 6G: Vision, enabling technologies, and applications," *IEEE J. Sel. Areas Commun.*, vol. 40, no. 1, pp. 5-36, Jan. 2022.
- [10] A. Affan, S. Mumtaz, H. M. Asif, and L. Musavian, "Performance analysis of Orbital Angular Momentum (OAM): A 6G waveform design," *IEEE Commun. Lett.*, vol. 25, no. 12, pp. 3985-3989, Dec. 2021.
- [11] A. R. Ndjiongue, T. M. N. Ngatched, O. A. Dobre, and H. Haas, "Re-configurable intelligent surface-based VLC receivers using tunable liquid-crystals: The concept," *J. Lightw. Technol.*, vol. 39, no. 10, pp. 3193-3200, May 2021.
- [12] L. Tosi, P. Rocca, N. Anselmi, and A. Massa, "Array antenna power pattern analysis through quantum computing," *IEEE Trans. Antennas Propag.*, vol. 71, no. 4, pp. 3251-3259, Apr. 2023.

- [13] S. Dash, C. Psomas, I. Krikidis, I. F. Akyildiz, and A. Pitsillides, "Active control of THz waves in wireless environments using graphene-based RIS," *IEEE Trans. Antennas Propag.*, vol. 70, no. 10, pp. 8785-8797, Oct. 2022.
- [14] W. Tang, M. Z. Chen, X. Chen, J. Y. Dai, Y. Han, M. Di Renzo, Y. Zeng, S. Jin, Q. Cheng, and T. J. Cui, "Wireless communications with reconfigurable intelligent surface: Path loss modeling and experimental measurement," *IEEE Trans. Wireless Commun.*, vol. 20, no. 1, pp. 421-439, Jan. 2021.
- [15] F. Yang, D. Erricolo and A. Massa, "Guest Editorial Smart Electromagnetic Environment," *IEEE Trans. Antennas Propag.*, vol. 70, no. 10, pp. 8687-8690, Oct. 2022.
- [16] M. Di Renzo, A. Zappone, M. Debbah, M.-S. Alouini, C. Yuen, J. de Rosny, and S. Tretyakov, "Smart radio environments empowered by reconfigurable intelligent surfaces: How it works, state of research, and the road ahead," *IEEE J. Sel. Areas Commun.*, vol. 38, no. 11, pp. 2450-2525, Nov. 2020.
- [17] M. Barbuto, Z. Hamzavi-Zarghani, M. Longhi, A. Monti, D. Ramaccia, S. Vellucci, A. Toscano, and F. Bilotti, "Metasurfaces 3.0: a new paradigm for enabling smart electromagnetic environments," *IEEE Trans. Antennas Propag.*, vol. 70, no. 10, pp. 8883-8897, Oct. 2022.
- [18] R. Flamini, D. De Donno, J. Gambini, F. Giuppi, C. Mazzucco, A. Milani, and L. Resteghini, "Towards a heterogeneous smart electromagnetic environment for millimeter-wave communications: An industrial viewpoint," *IEEE Trans. Antennas Propag.*, vol. 70, no. 10, pp. 8898-8910, Oct. 2022.
- [19] J. R. Kazim, J. Watt, T. J. Cui, A. Zoha, L. Li, S. A. Shah, A. Alomainy, M. A. Imran, and Q. H. Abbasi, "Wireless on walls: Revolutionizing the future of health care," *IEEE Antennas Propag. Mag.*, vol. 63, no. 6, pp. 87-93, Dec. 2021.
- [20] F. Naeem, G. Kaddoum, S. Khan, K. S. Khan, and N. Adam, "IRS-Empowered 6G networks: Deployment strategies, performance optimization, and future research directions," *IEEE Access*, vol. 10, pp. 118676-118696, 2022.

- [21] M. Salucci and A. Massa, "Unconventional sources for smart EM environments: An inverse scattering vision," *Reviews of Electromagnetics*, Invited Paper, vol. 1, pp. 17-18, 2022.
- [22] A. Massa, A. Benoni, P. Da R , S. K. Goudos, B. Li, G. Oliveri, A. Polo, P. Rocca, and M. Salucci, "Designing smart electromagnetic environments for next-generation wireless communications," *Telecom*, vol. 2, no. 2, pp. 213-221, May 2021.
- [23] M. Salucci, A. Benoni, G. Oliveri, P. Rocca, B. Li, and A. Massa, "A multi-hop strategy for the planning of EM skins in a smart electromagnetic environment," *IEEE Trans. Antennas Propag.*, vol. 71, no. 3, pp. 2758-2767, Mar. 2023.
- [24] G. Oliveri, F. Zardi, P. Rocca, M. Salucci, and A. Massa, "Constrained-design of passive static EM skins," *IEEE Trans. Antennas Propag.*, vol. 71, no. 2, pp. 1528-1538, Feb. 2023.
- [25] G. Oliveri, P. Rocca, M. Salucci, and A. Massa, "Holographic smart EM skins for advanced beam power shaping in next generation wireless environments," *IEEE J. Multiscale Multiphys. Comput. Tech.*, vol. 6, pp. 171-182, Nov. 2021.
- [26] G. Oliveri, F. Zardi, P. Rocca, M. Salucci, and A. Massa, "Building a Smart EM Environment - AI-Enhanced aperiodic micro-scale design of passive EM skins," *IEEE Trans. Antennas Propag.*, vol. 70, no. 10, pp. 8757-8770, Oct. 2022.
- [27] P. Rocca, P. Da R , N. Anselmi, M. Salucci, G. Oliveri, D. Erricolo, and A. Massa, "On the design of modular reflecting EM skins for enhanced urban wireless coverage," *IEEE Trans. Antennas Propag.*, vol. 70, no. 10, pp. 8771-8784, Oct. 2022.
- [28] A. Benoni, M. Salucci, G. Oliveri, P. Rocca, B. Li, and A. Massa, "Planning of EM skins for improved quality-of-service in urban areas," *IEEE Trans. Antennas Propag.*, vol. 70, no. 10, pp. 8849-8862, Oct. 2022.
- [29] V. Degli-Esposti, E. M. Vitucci, M. Di Renzo, and S. Tretyakov, "Reradiation and Scattering from a reconfigurable intelligent surface: A general macroscopic model," *IEEE Trans. Antennas Propag.*, vol. 70, no. 10, pp. 8691-8706, Oct. 2022.

- [30] Z. Zhang, J. W. Zhang, J. W. Wu, J. C. Liang, Z. X. Wang, Q. Cheng, Q. S. Cheng, T. J. Cui, H. Q. Yang, G. B. Liu, and S. R. Wang, "Macromodeling of reconfigurable intelligent surface based on microwave network theory," *IEEE Trans. Antennas Propag.*, vol. 70, no. 10, pp. 8707-8717, Oct. 2022.
- [31] P. Mei, Y. Cai, K. Zhao, Z. Ying, G. F. Pedersen, X. Q. Lin, and S. Zhanget, "On the study of reconfigurable intelligent surfaces in the near-field region," *IEEE Trans. Antennas Propag.*, vol. 70, no. 10, pp. 8718-8728, Oct. 2022.
- [32] J. C. Liang, Y. Gao, C. Xiao, S. Gao, L. Zhang, S. Jin, and T. J. Cui, "An angle-insensitive 3-bit reconfigurable intelligent surface," *IEEE Trans. Antennas Propag.*, vol. 70, no. 10, pp. 8798-8808, Oct. 2022.
- [33] G. Oliveri, P. Rocca, M. Salucci, D. Erricolo, and A. Massa, "Multi-scale single-bit RP-EMS synthesis for advanced propagation manipulation through System-by-Design," *IEEE Trans. Antennas Propag.*, vol. 70, no. 10, pp. 8809-8824, Oct. 2022.
- [34] G. Stratidakis, S. Droulias, and A. Alexiou, "Optimal position and orientation study of reconfigurable intelligent surfaces in a mobile user environment," *IEEE Trans. Antennas Propag.*, vol. 70, no. 10, pp. 8863-8871, Oct. 2022.
- [35] W. Tang, X. Chen, M. Z. Chen, J. Y. Dai, Y. Han, M. Di Renzo, S. Jin, Q. Cheng, and T. J. Cui, "Path loss modeling and measurements for reconfigurable intelligent surfaces in the millimeter-wave frequency band," *IEEE Trans. Commun.*, vol. 70, no. 9, pp. 6259-6276, Sep. 2022.
- [36] M. Lodro, J.-B. Gros, S. Greedy, G. Lerosey, A. Al Rawi, and G. Gradoni, "Experimental evaluation of multi-operator RIS-assisted links in indoor environment," arXiv:2206.07788 [eess.SP], Jun. 2022.
- [37] J. Rains, J. R. Kazim, A. Tukmanov, T. J. Cui, L. Zhang, Q. H. Abbasi, and M. A. Imran, "High-resolution programmable scattering for wireless coverage enhancement: An indoor field trial campaign," arXiv:2112.11194, Jul. 2022.

- [38] L. Dai, B. Wang, M. Wang, X. Yang, J. Tan, S. Bi, S. Xu, F. Yang, Z. Chen, M. Di Renzo, C.-B. Chae, and L. Hanzo, "Reconfigurable intelligent surface-based wireless communications: Antenna design, prototyping, and experimental results," *IEEE Access*, vol. 8, pp. 45913-45923, 2020.
- [39] J. Sang, Y. Yuan, W. Tang, Y. Li, X. Li, S. Jin, Q. Cheng, and T. J. Cui, "Coverage enhancement by deploying RIS in 5G commercial mobile networks: Field trials," *IEEE Trans. Wireless Commun.*, 2023, doi: 10.1109/MWC.011.2200356.
- [40] X. Pei, H. Yin, L. Tan, L. Cao, Z. Li, K. Wang, K. Zhang, and E. Bjornson, "RIS-Aided wireless communications: Prototyping, adaptive beamforming, and indoor/outdoor field trials," *IEEE Trans. Commun.*, vol. 69, no. 12, pp. 8627- 8640, Dec. 2021.
- [41] G. C. Trichopoulos, P. Theofanopoulos, B. Kashyap, A. Shekhawat, A. Modi, T. Osman, S. Kumar, A. Sengar, A. Chang, and A. Alkhateeb, "Design and evaluation of reconfigurable intelligent surfaces in real-world environment," *IEEE Open J. Commun. Soc.*, vol. 3, pp. 462-474, 2022.
- [42] C. Liu, F. Yang, S. Xu, and M. Li, "Reconfigurable metasurface: A systematic categorization and recent advances," arXiv:2301.00593 [physics.app-ph], Jan. 2023.
- [43] G. C. Alexandropoulos, N. Shlezinger, and P. Del Hougne, "Reconfigurable intelligent surfaces for rich scattering wireless communications: Recent experiments, challenges, and opportunities," *IEEE Commun. Mag.*, vol. 59, no. 6, pp. 28-34, 2021.
- [44] M. M. Amri, N. M. Tran, and K. W. Choi, "Reconfigurable intelligent surface-aided wireless communications: Adaptive beamforming and experimental validations," *IEEE Access*, vol. 9, pp. 147442-147457, 2021.
- [45] Altair Winprop 2020, Altair Engineering, Inc., www.altairhyperworks.com/feko
- [46] D. K. Christensen, "The total cost of ownership," *Facilities Manager*, vol. 32, no. 4, pp. 20-31, Jul./Aug. 2016.

- [47] J. Huang and J. A. Encinar, *Reflectarray Antennas*. Hoboken, NJ: Wiley-Interscience, 2008.
- [48] ANSYS Electromagnetics Suite - HFSS (2021). ANSYS, Inc.
- [49] C. Balanis, *Antenna theory: analysis and design*. Hoboken, N.J.: Wiley, 2016.
- [50] Data Sheet Aruba 300 Series Wireless Access Point [Online]. Available: https://www.arubanetworks.com/assets/ds/DS_AP300Series.pdf.
- [51] Araknis Networks, Wi-Fi Best Practices [Online]. Available: <https://www.control4.com/docs/product/networking/wi-fi-best-practices/english/latest//networking-wi-fi-best-practices-rev-a.pdf>
- [52] OOKLA Speedtest[®] [Online]. Available: <https://www.speedtest.net>

FIGURE CAPTIONS

- **Figure 1.** Picture of the large-scale test-bed situated in *Mesiano* building of the Department of Civil, Environmental, and Mechanical Engineering (*DICAM*) of the University of Trento, Trento (Italy).
- **Figure 2.** *Reference Scenario* - Color-map of the (a) *RT*-simulated and (b) measured received power distributions at a constant height of $h = 1.2$ [m] (Fig. 3) within the common places (i.e., hallways “A”, “B”, “C”, “D”, and “E”) of the second floor of the *Mesiano* building (Fig. 1).
- **Figure 3.** Sketch of the measurement geometry.
- **Figure 4.** *Reference Scenario* (Hallway “A”) - Plot of (a) the simulated received power distribution and (b) the corresponding thresholded ($P_{th} = -65$ [dBm]) binary-map.
- **Figure 5.** *Reference Scenario* ($P_{th} = -65$ [dBm]) - Thresholded binary-map of the (a) *RT*-simulated and (b) measured received power distributions within the common places of the second floor of the *Mesiano* building.
- **Figure 6.** Picture of (a) the hallway “A” where the floor has been marked with paper scotch tape in correspondence with the uniform sampling grid and (b) the hand-held smartphone used in the measurement campaign.
- **Figure 7.** *Reference Scenario* (Hallway “A”) - Plot of (a) the measured received power distribution and (b) the corresponding thresholded ($P_{th} = -65$ [dBm]) binary-map.
- **Figure 8.** *SEME Scenario* (Hallway “A”) - Geometrical sketch of the *SP-EMS* deployment: (a) global 3-D view and (b) zoom in the area where both the *AP* (Ψ_A) and the *SP-EMS* (\mathcal{S}_A) are located.
- **Figure 9.** Sketch of the layout of the synthesized dual-layers *SP-EMS*s for (a) the hallways “A” and “B” and (b) the hallway “C”.
- **Figure 10.** *SEME Scenario* (Hallway “A”) - Plot of (a) the *CDF* of the received power, Θ , and (b) the *RoI* reduction, $\rho(\Omega_A)$, versus the *SP-EMS* side, L_A .

- **Figure 11.** *SEME Scenario* (Hallway “A”) - Full-wave simulated directivity pattern of the *SP-EMS* \mathcal{S}_A in Fig. 9(a) of side-length $L_A = 0.55$ [m].
- **Figure 12.** *SEME Scenario* (Hallway “A”, $L_A = 0.55$ [m]) - Plot of (a) the simulated received power distribution, (b) the corresponding thresholded ($P_{th} = -65$ [dBm]) binary-map, and (c) the received power improvement with respect to the “reference” scenario, ΔP_{RX} .
- **Figure 13.** *SEME Scenario* (Hallway “B”, $L_B = 0.55$ [m]) - Plot of (a) the difference map, ΔP_{RX} , and (b) the *CDF* of the received power, Θ .
- **Figure 14.** *SEME Scenario* (Hallway “C”, $L_C = 0.32$ [m]) - Plot of (a) the difference map, ΔP_{RX} , and (b) the *CDF* of the received power, Θ .
- **Figure 15.** *SEME Scenario* (Hallway “C”) - Geometrical sketch of the *SP-EMS* deployment: (a) global 3-D view and (b) zoom in the area where both the *AP* (Ψ_C) and the *SP-EMS* (\mathcal{S}_C) are located.
- **Figure 16.** *SEME Scenario* (Hallway “A”, $L_A = 0.55$ [m]) - Pictures of (a) the sketch of the *EMS* positioning errors, Δy and Δz , (b) the map of the *RoI* reduction, $\rho(\Omega_A)$, versus $(\Delta y, \Delta z) \in [-0.1, 0.1]$ [m], (c) the plot of the simulated *CDF* in correspondence with (c) horizontal ($\Delta z = 0$ [m], $\Delta y \in [-0.1, 0.1]$ [m]) or (d) vertical ($\Delta y = 0$ [m], $\Delta z \in [-0.1, 0.1]$ [m]) displacements of the nominal location of the *EMS* \mathcal{S}_A .
- **Figure 17.** *SEME Scenario* (Hallway “A”, $L_A = 0.55$ [m]) - Picture of (a) the fabricated prototype of the *SP-EMS* layout in Fig. 9(a) and (b) the real deployment according to Fig. 8.
- **Figure 18.** *SEME Scenario* (Hallway “A”, $L_A = 0.55$ [m]) - Plot of (a) the measured received power distribution and (b) the measured received power improvement with respect to the “reference” scenario, ΔP_{RX} .
- **Figure 19.** *SEME Scenario* (Hallway “A”, $L_A = 0.55$ [m]) - Plot of both the simulated and the measured *CDFs* of the received power (i.e., Θ and $\tilde{\Theta}$).

- **Figure 20.** Screenshot of the OOKLA Speedtest[®] [52] for (a)(c) the download and (b)(d) the upload links in (a)(b) the “reference” scenario and (c)(d) the *SEME* ($L_A = 0.55$ [m]) one at the same throughput-peak time-instant.

TABLE CAPTIONS

- **Table I.** *SEME Scenario* (Hallway “A”) - Coverage-performance indexes in correspondence with different side-lengths of the *SP-EMS* \mathcal{S}_A in Fig. 9(a).
- **Table II.** *SEME Scenario* (Hallways “B”, “C”, “D”, “E”) - Coverage-performance indexes.
- **Table III.** OOKLA Speedtest[®] [52] statistics.
- **Table IV.** *TCO*-analysis indexes.



Fig. 1 - A. Benoni et al., “Towards Real-World Indoor Smart ...”

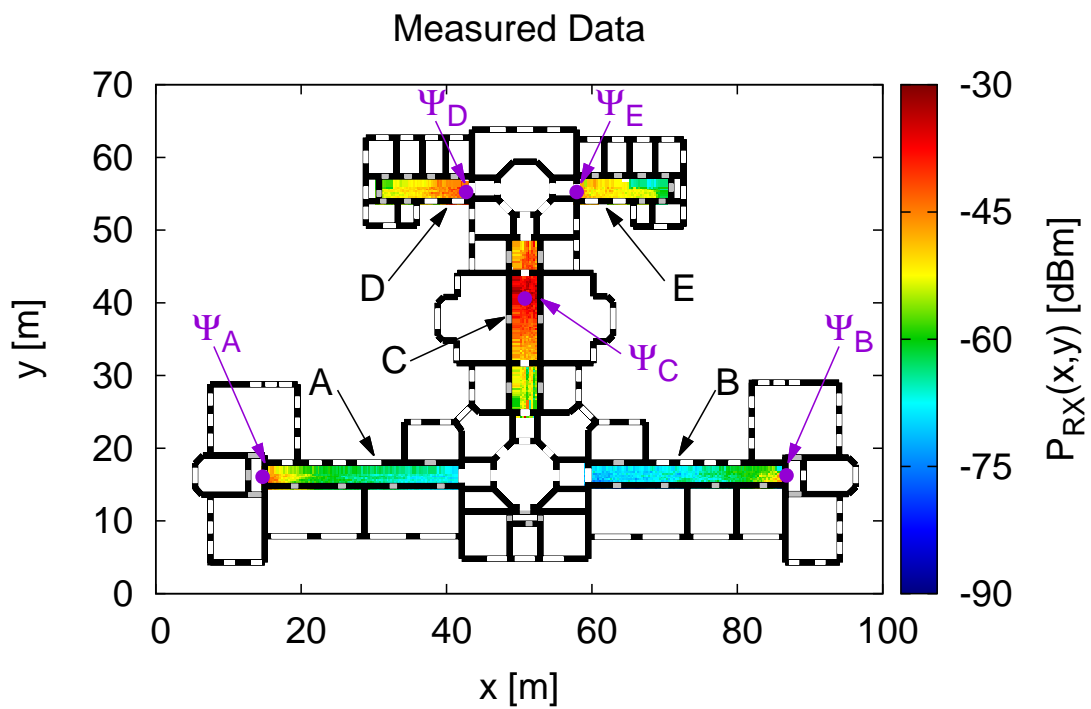
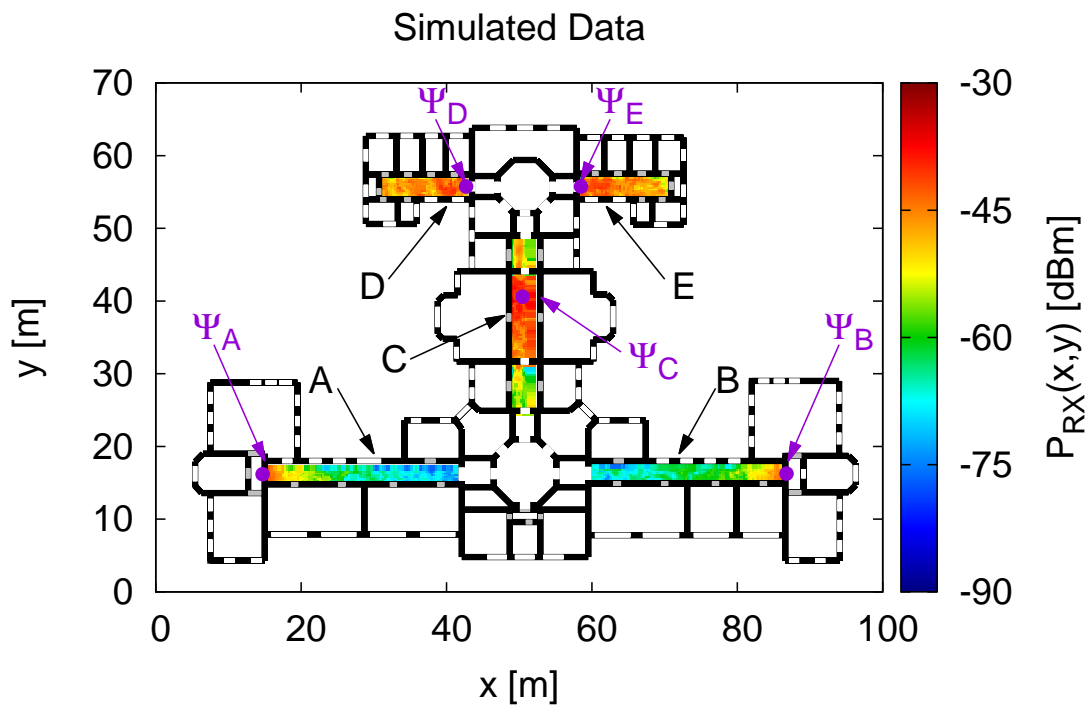


Fig. 2 - A. Benoni et al., "Towards Real-World Indoor Smart ..."

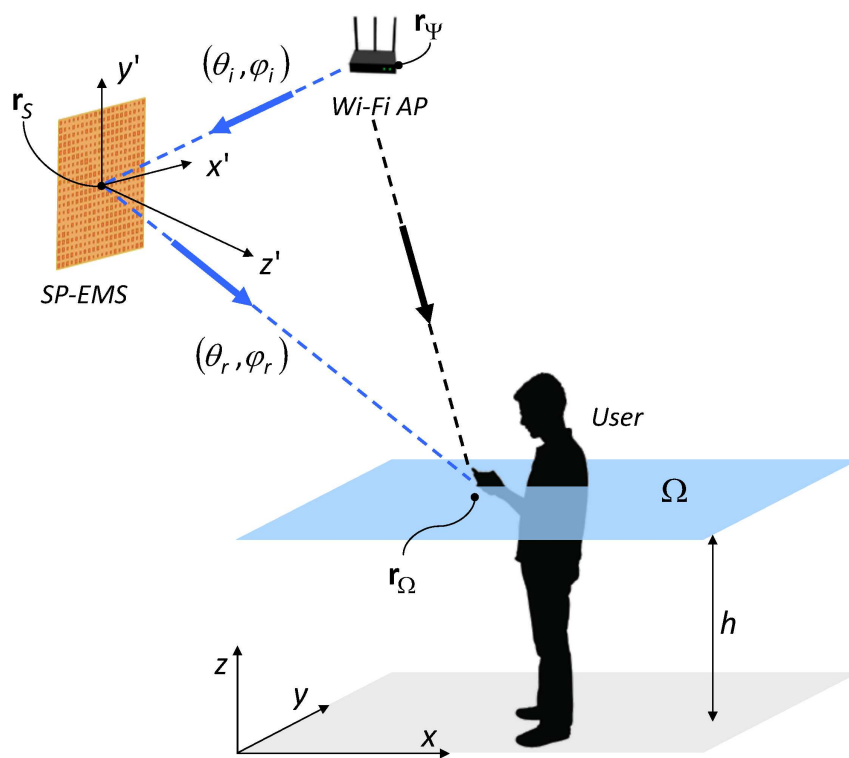
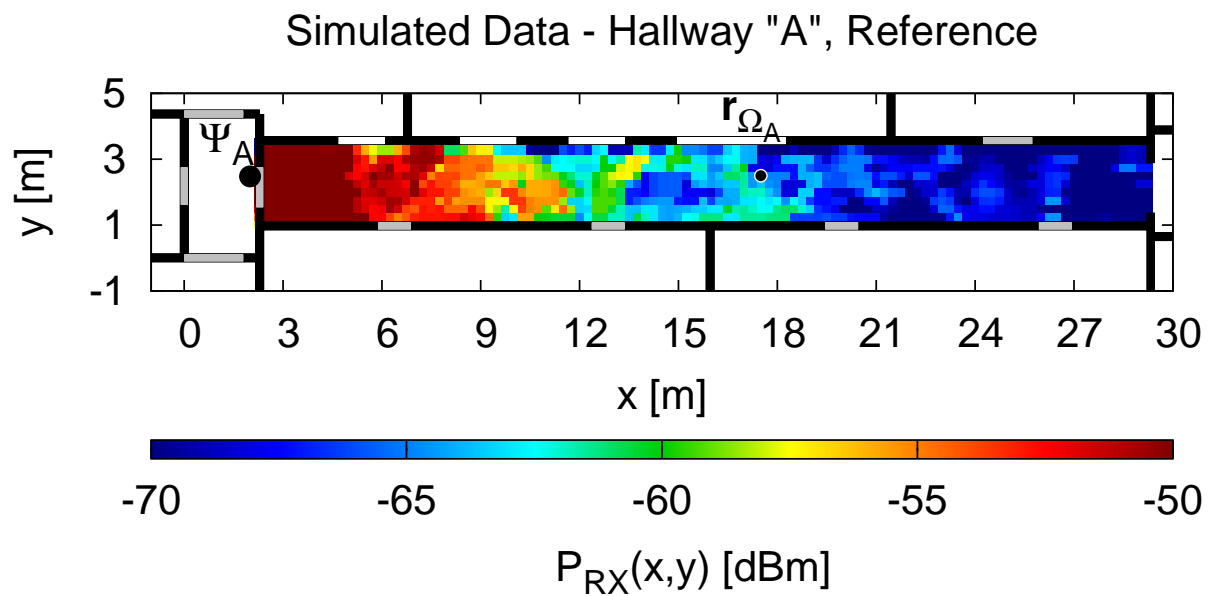
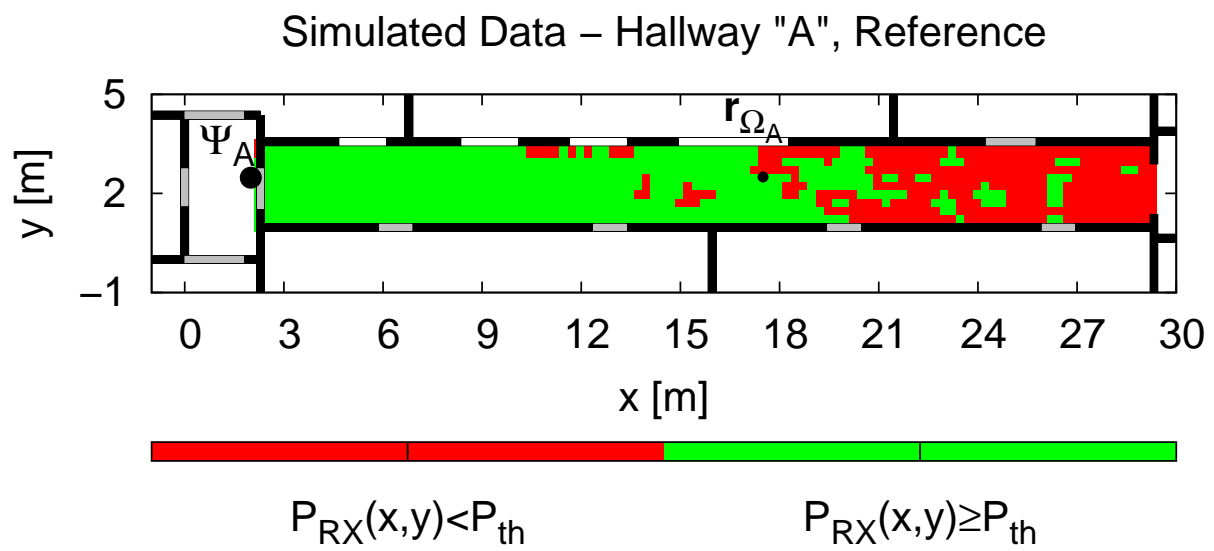


Fig. 3 - A. Benoni et al., “Towards Real-World Indoor Smart ...”



(a)



(b)

Fig. 4 - A. Benoni et al., "Towards Real-World Indoor Smart ..."

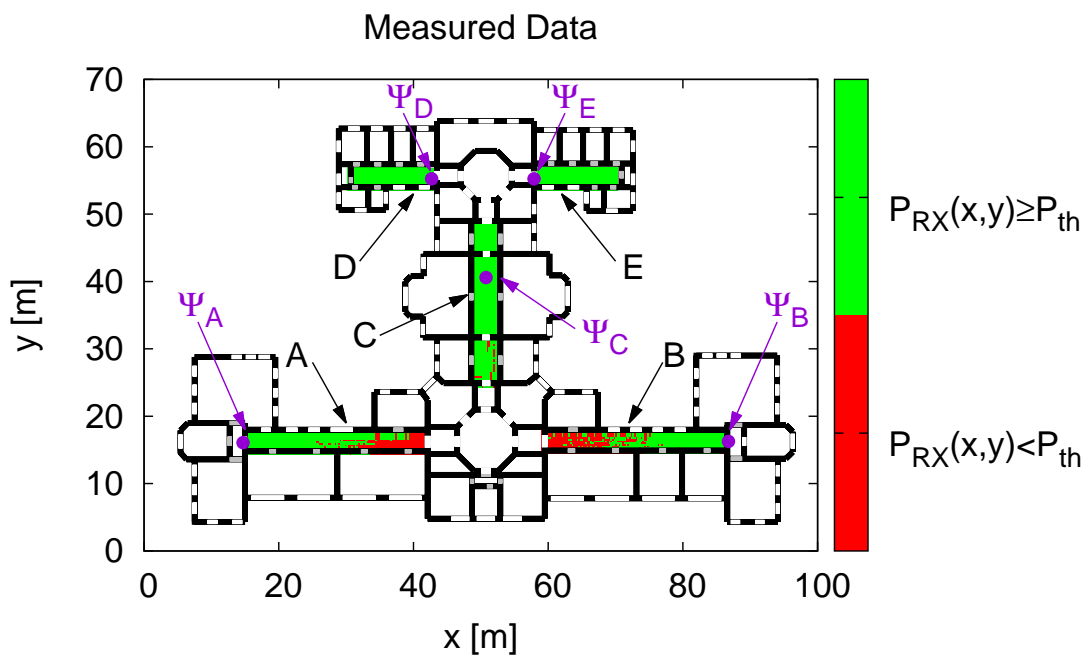
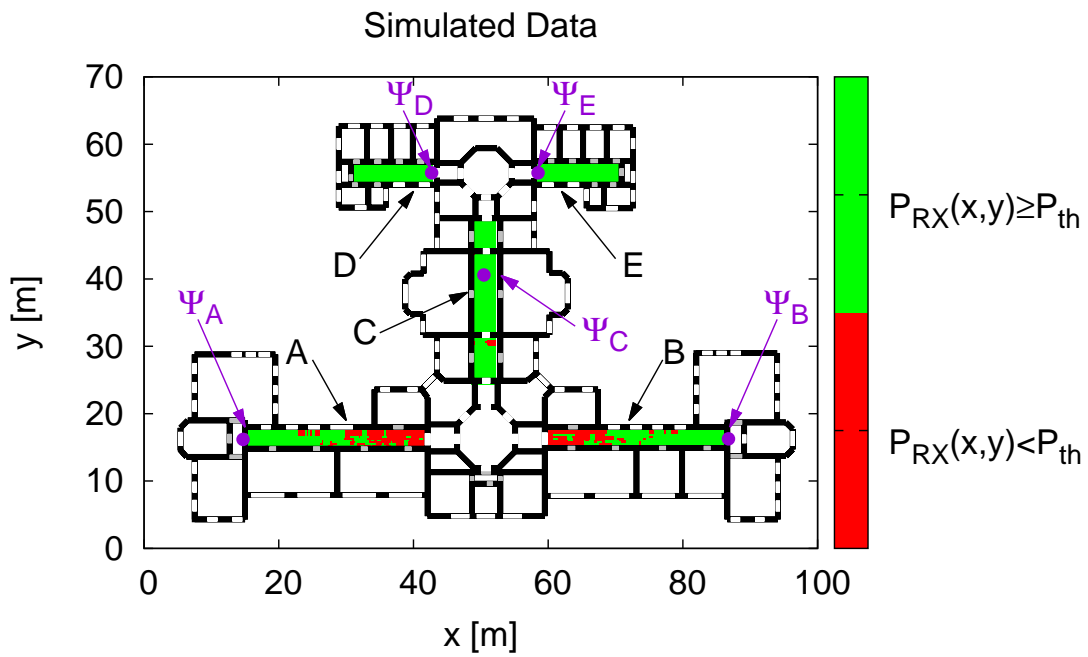
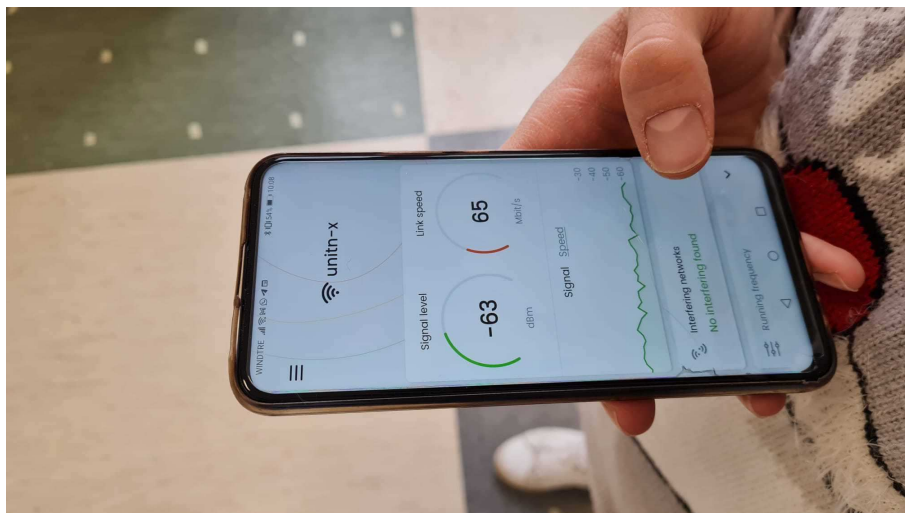


Fig. 5 - A. Benoni et al., "Towards Real-World Indoor Smart ..."

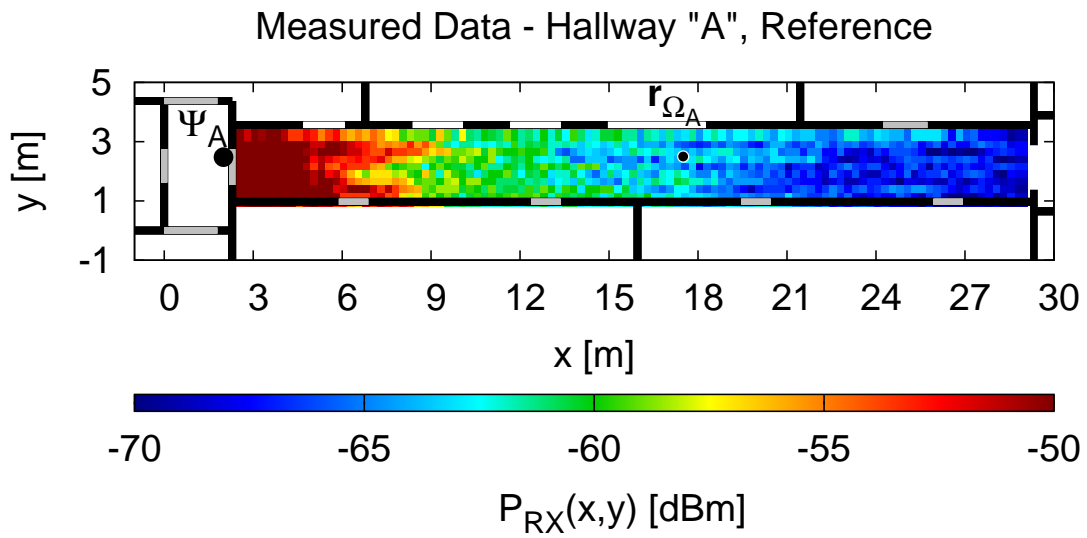


(a)

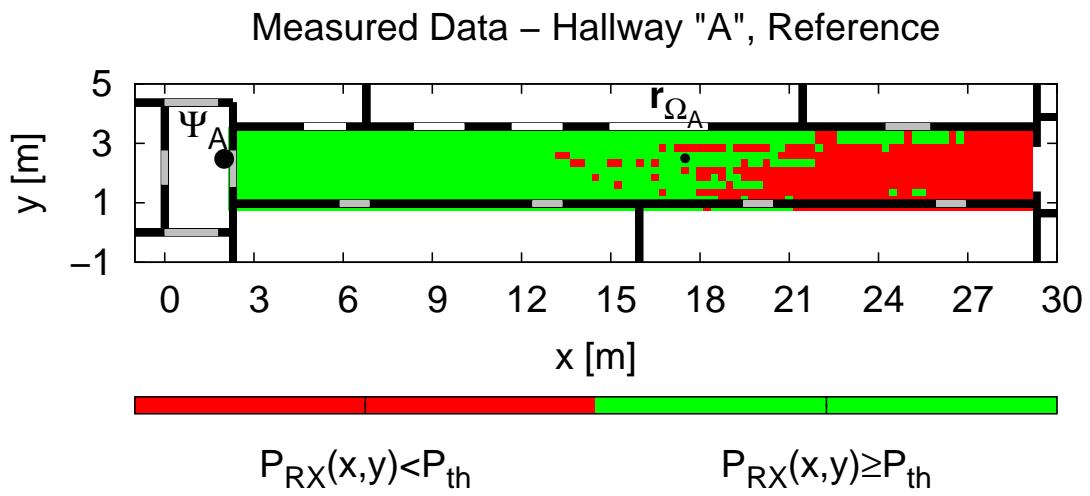


(b)

Fig. 6 - A. Benoni et al., “Towards Real-World Indoor Smart ...”

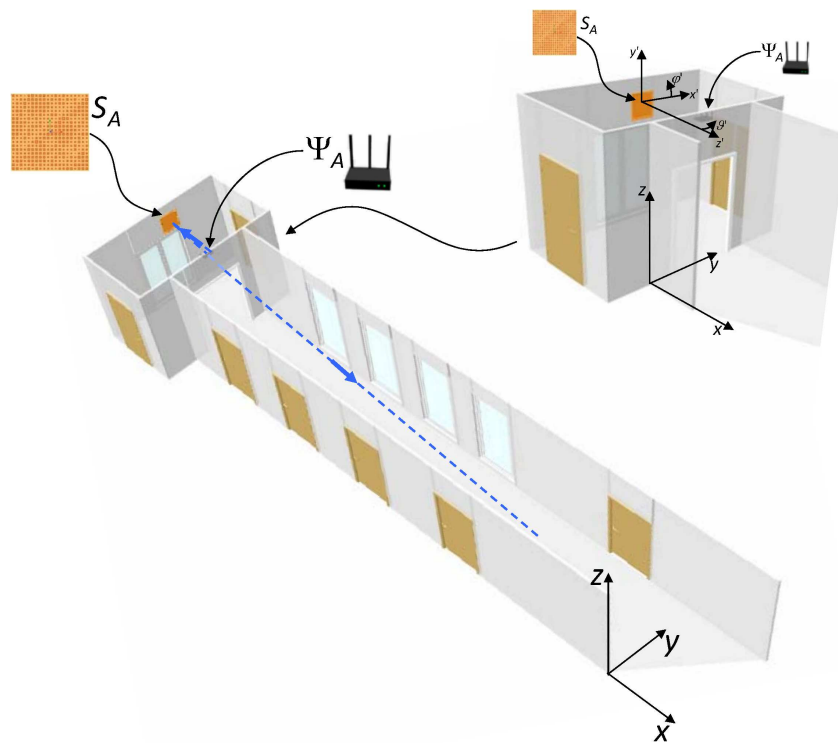


(a)

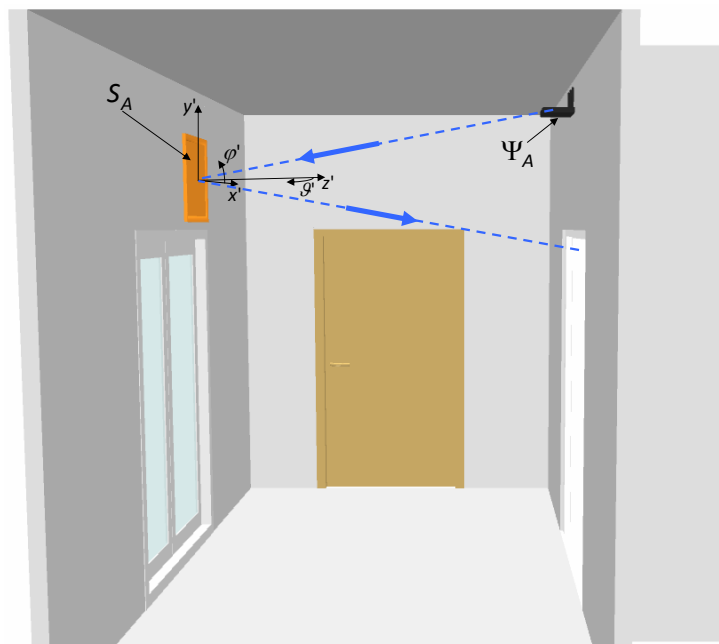


(b)

Fig. 7 - A. Benoni et al., "Towards Real-World Indoor Smart ..."

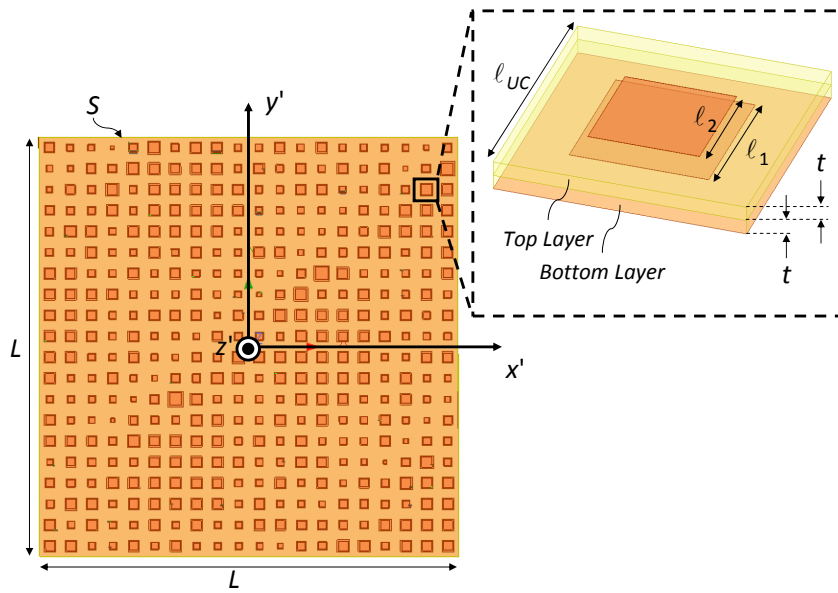


(a)

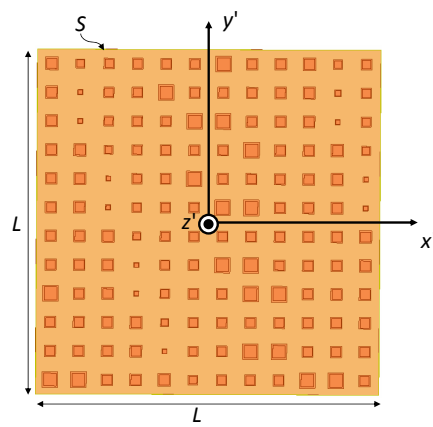


(b)

Fig. 8 - A. Benoni et al., "Towards Real-World Indoor Smart ..."

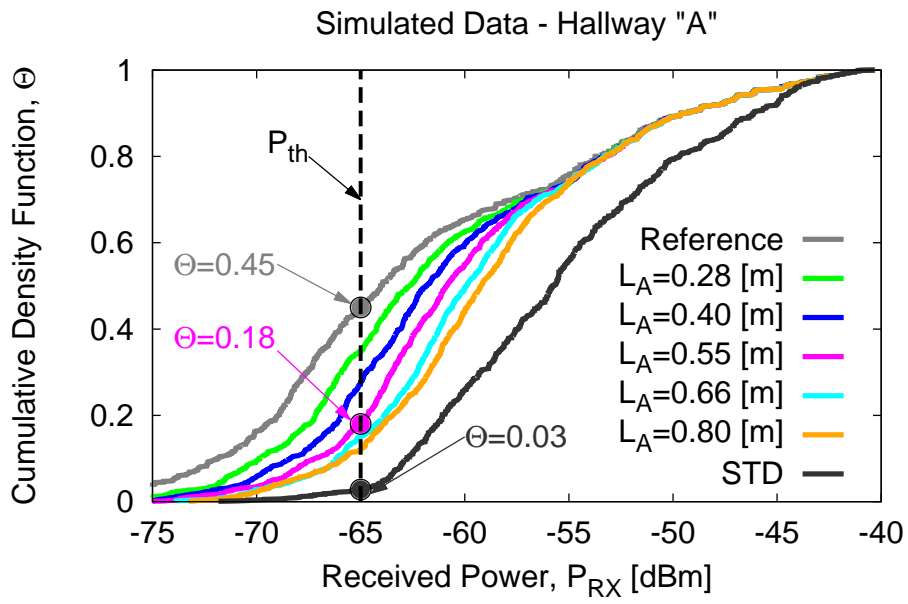


(a)

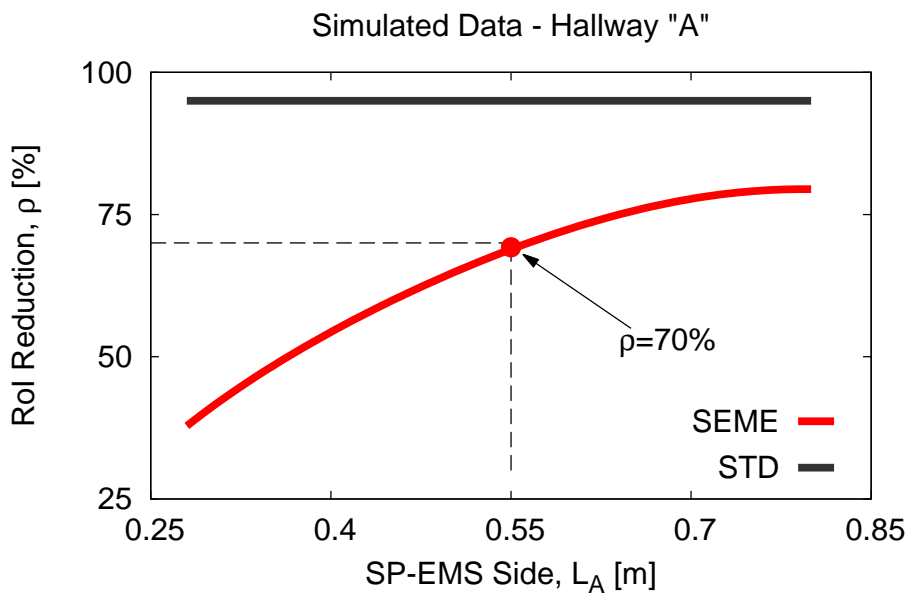


(b)

Fig. 9 - A. Benoni et al., “Towards Real-World Indoor Smart ...”



(a)



(b)

Fig. 10 - A. Benoni et al., "Towards Real-World Indoor Smart ..."

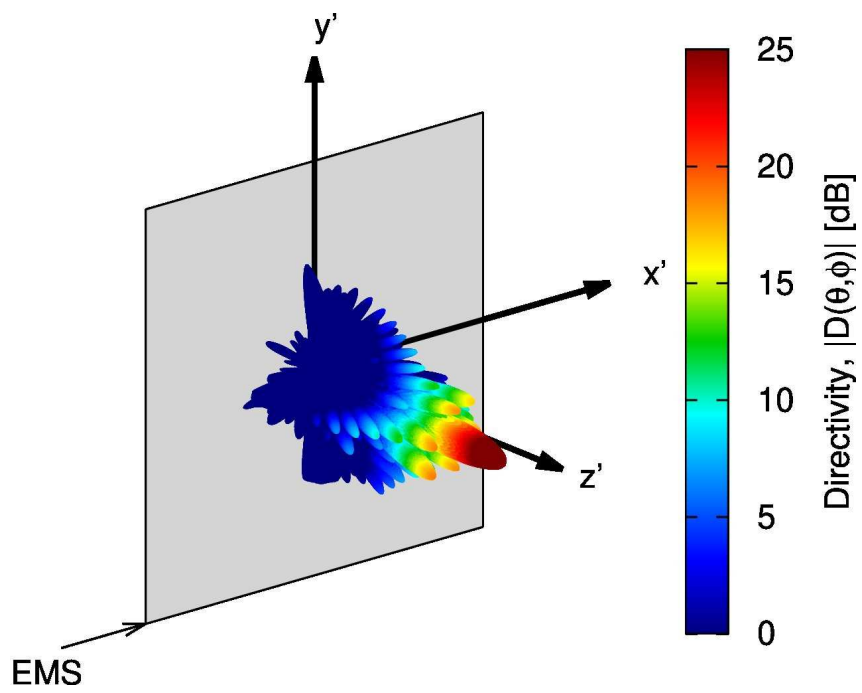
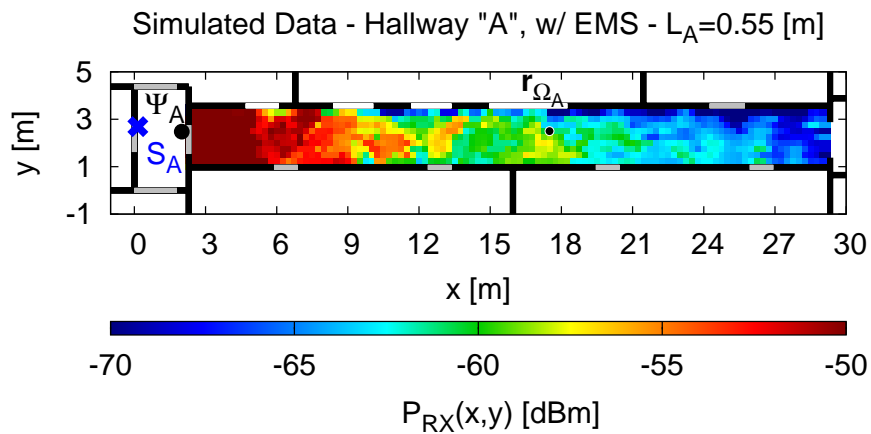
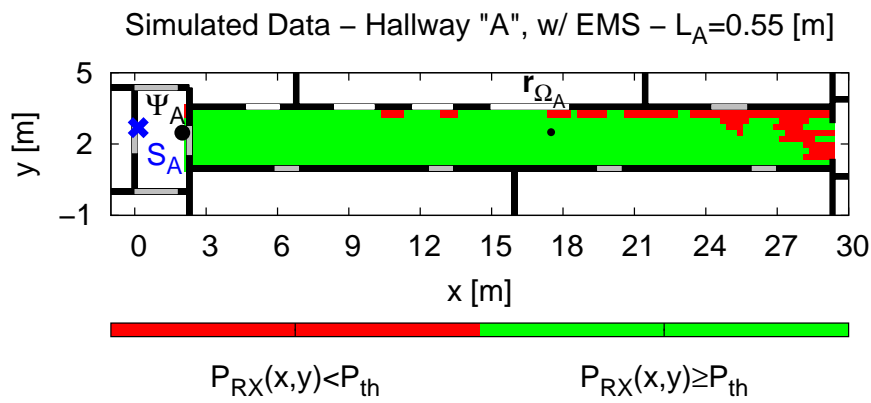


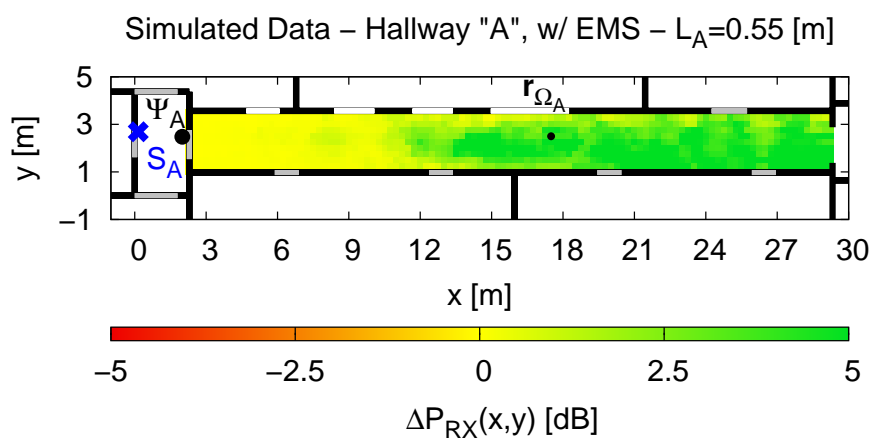
Fig. 11 - A. Benoni et al., "Towards Real-World Indoor Smart ..."



(a)



(b)



(c)

Fig. 12 - A. Benoni et al., "Towards Real-World Indoor Smart ..."

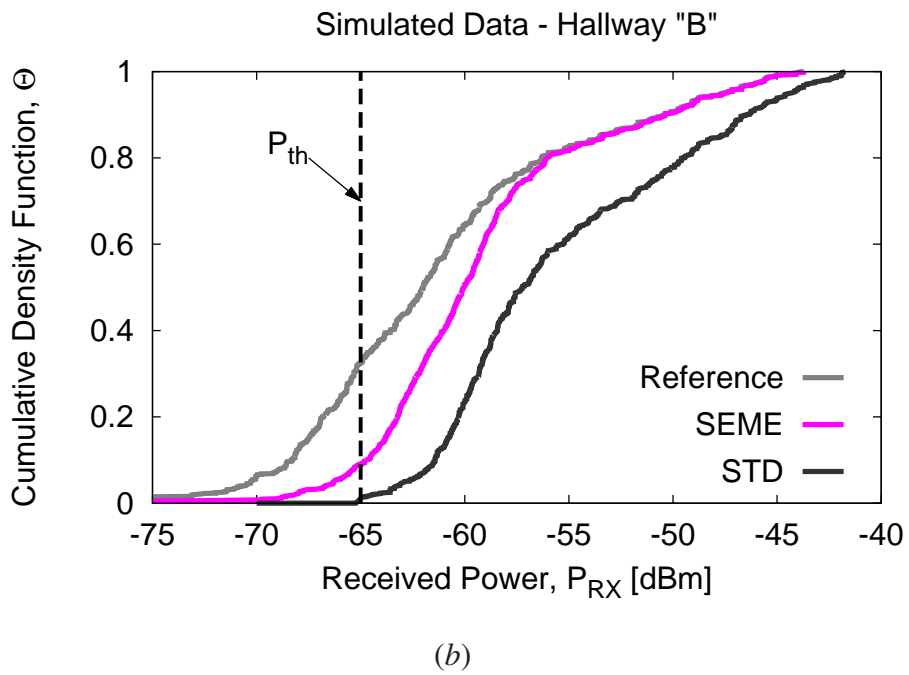
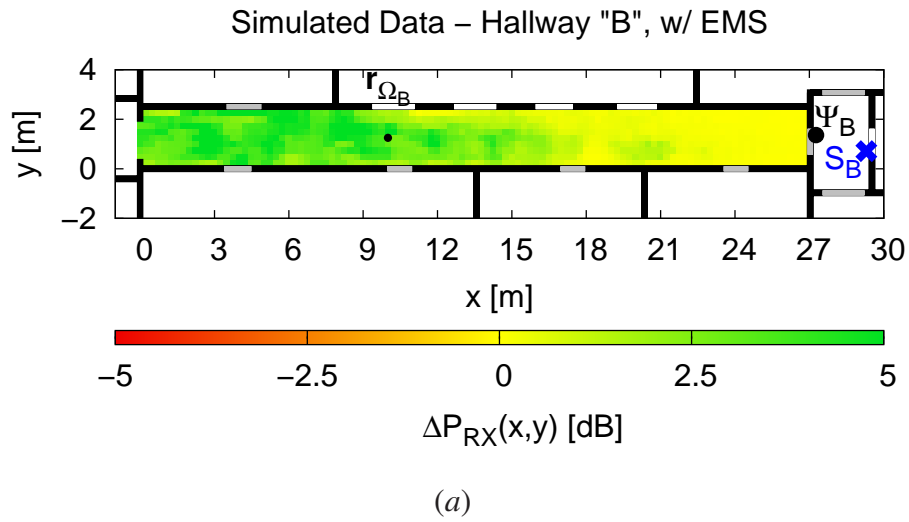
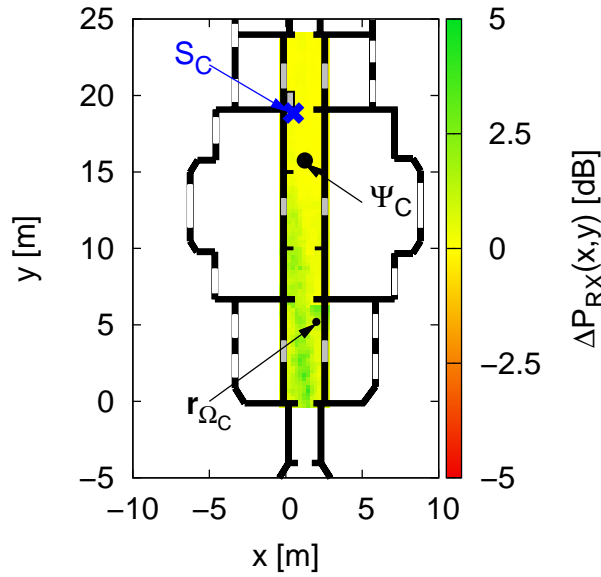


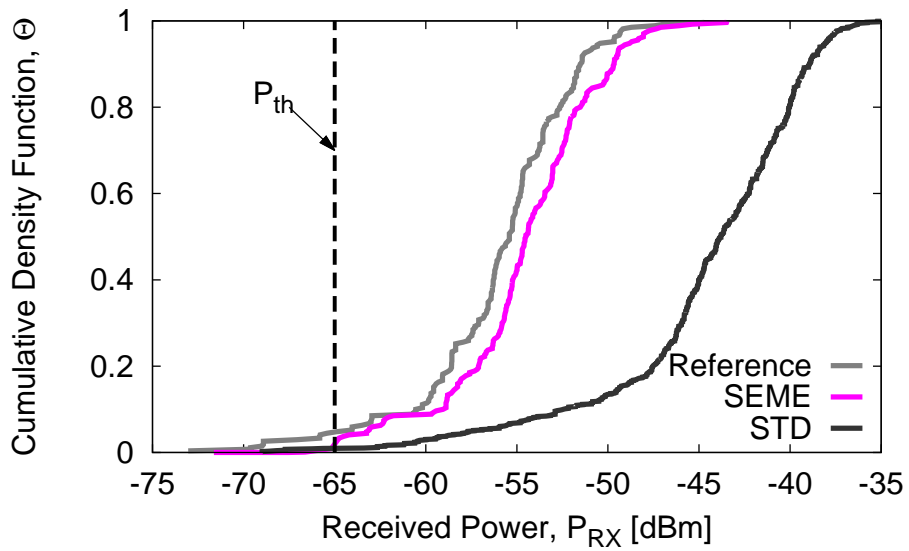
Fig. 13 - A. Benoni et al., “Towards Real-World Indoor Smart ...”

Simulated Data – Hallway "C", w/ EMS



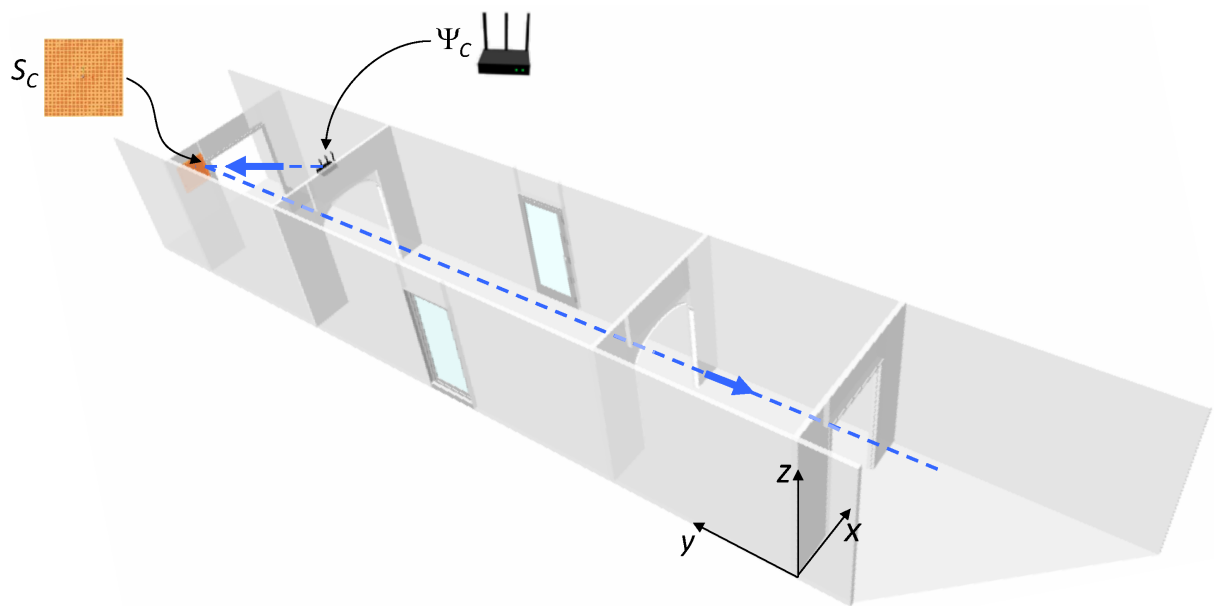
(a)

Simulated Data - Hallway "C"

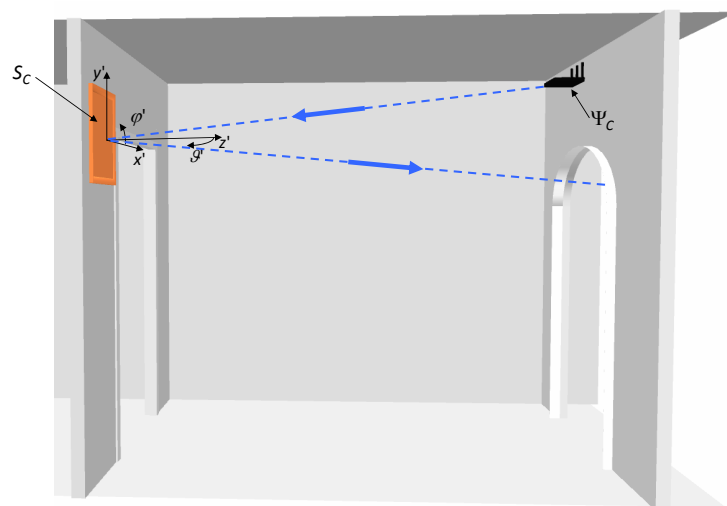


(b)

Fig. 14 - A. Benoni et al., "Towards Real-World Indoor Smart ..."

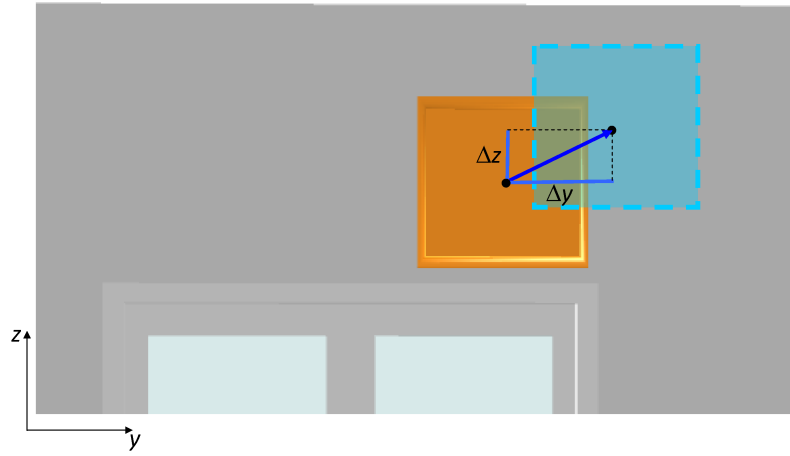


(a)

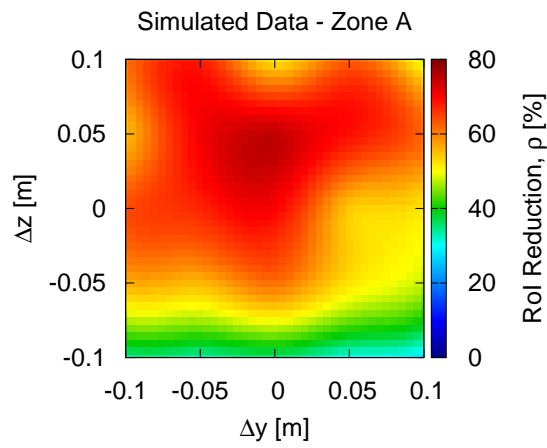


(b)

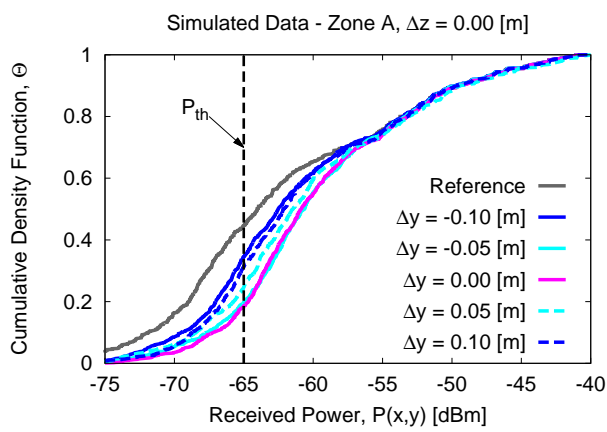
Fig. 15 - A. Benoni et al., "Towards Real-World Indoor Smart ..."



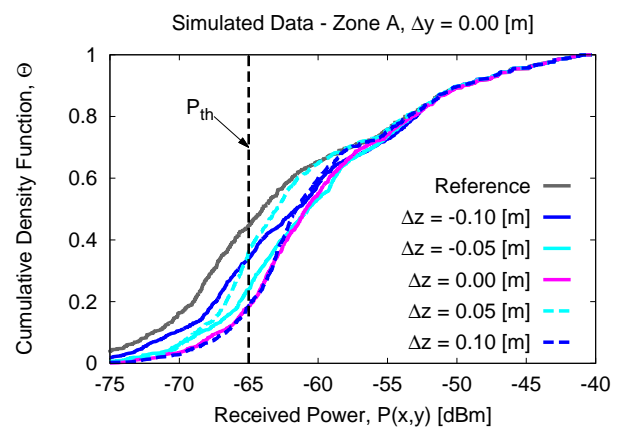
(a)



(b)

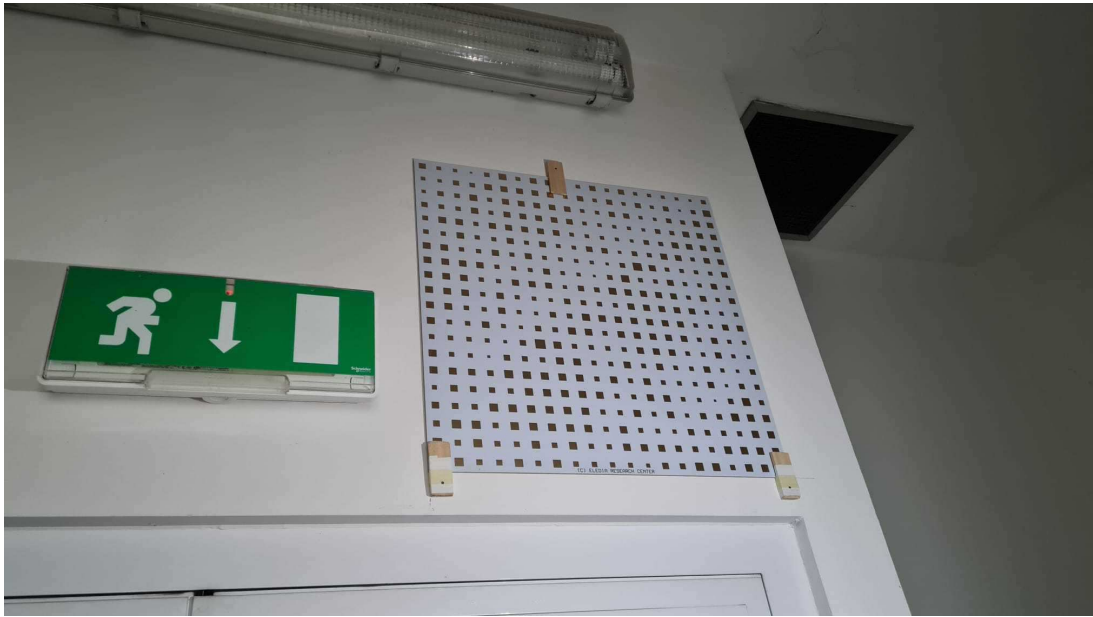


(c)

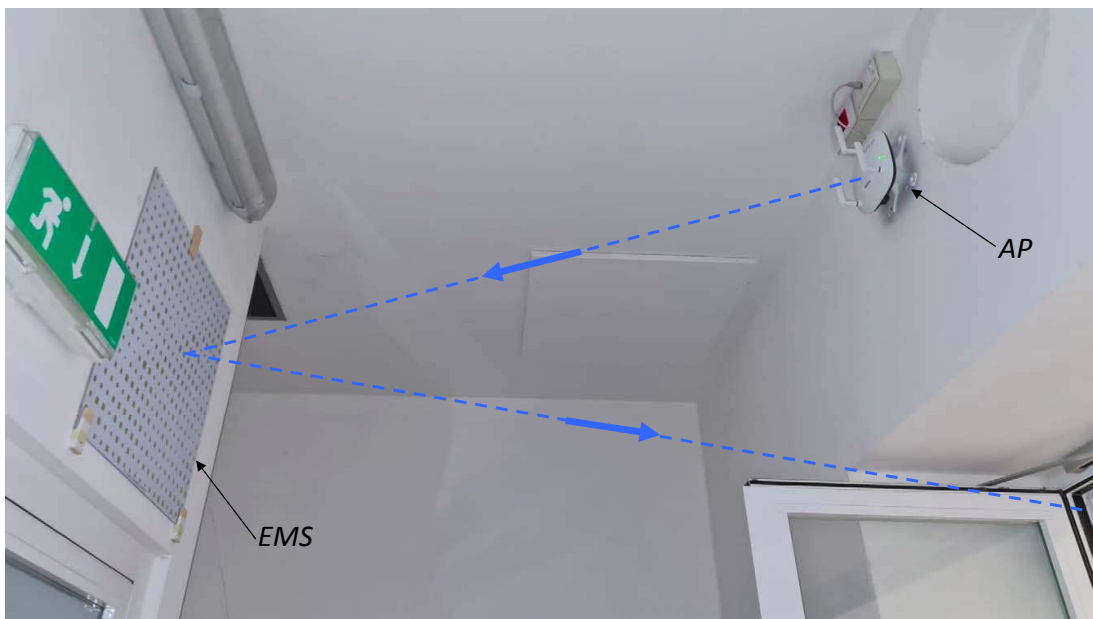


(d)

Fig. 16 - A. Benoni et al., “Towards Real-World Indoor Smart ...”

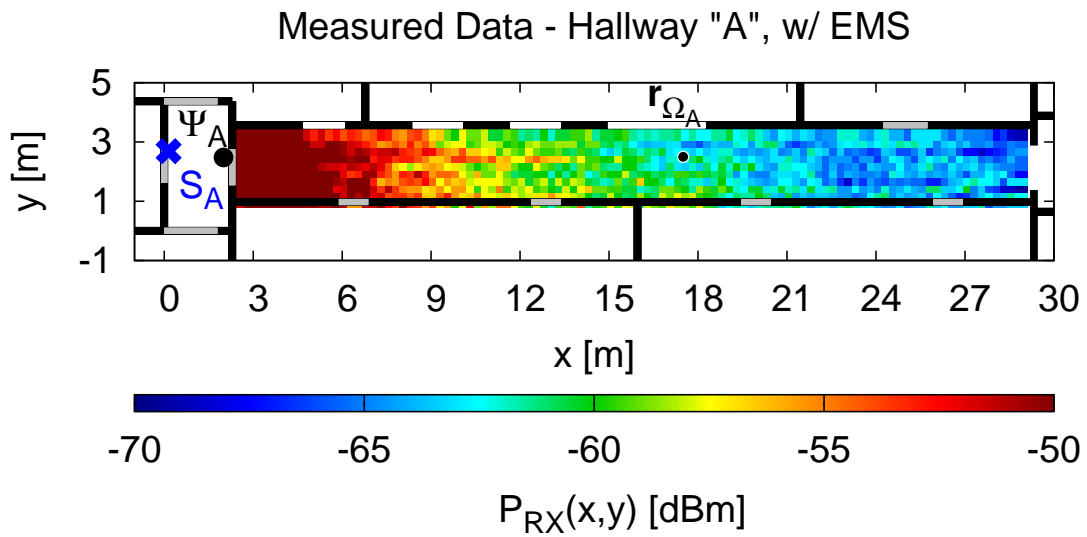


(a)

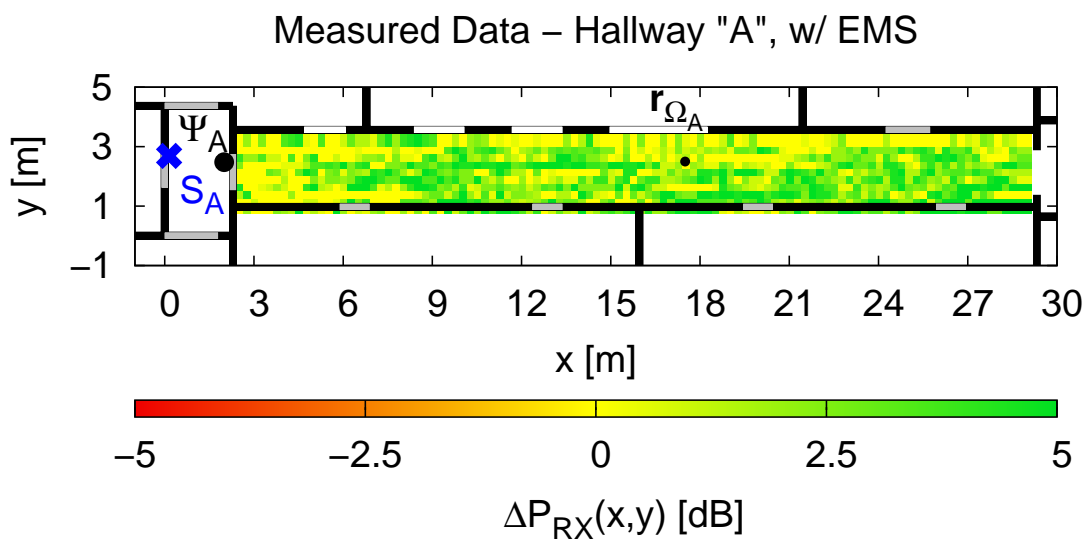


(b)

Fig. 17 - A. Benoni et al., "Towards Real-World Indoor Smart ..."



(a)



(b)

Fig. 18 - A. Benoni et al., "Towards Real-World Indoor Smart ..."

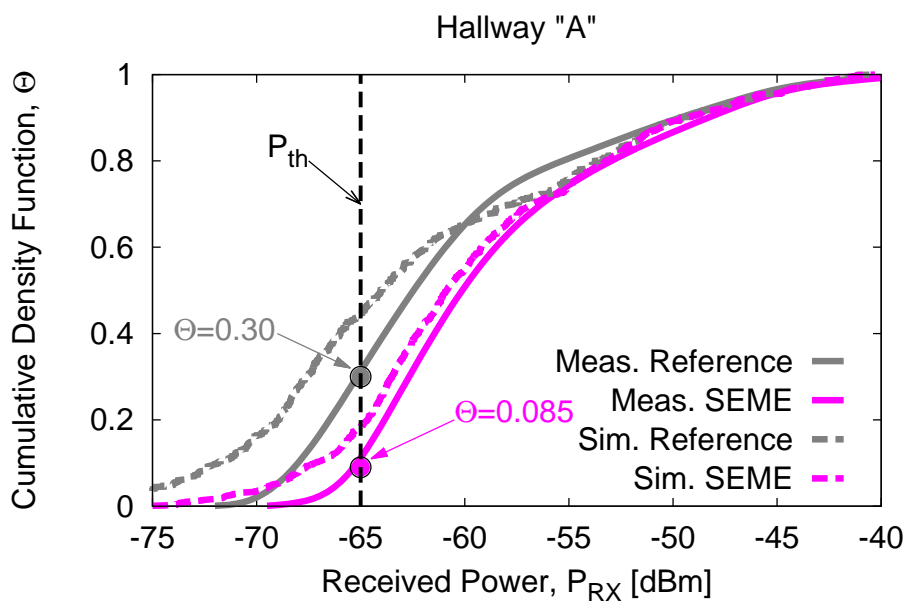


Fig. 19 - A. Benoni et al., "Towards Real-World Indoor Smart ..."



Fig. 20 - A. Benoni et al., “Towards Real-World Indoor Smart ...”

<i>EMS Side</i>	<i>RoI Area</i>	<i>RoI Reduction</i>	ΔP_{RX}^{\min}	ΔP_{RX}^{\max}	$\Delta P_{RX}^{\text{avg}}$	$\Delta P_{RX}^{\text{dev}}$
L_A [m]	$\Lambda_{SEME}(\Omega_A)$ [m ²]	$\rho(\Omega_A)$ [%]	[dB]	[dB]	[dB]	[dB]
0.28	14.38	38.84	0.00	5.74	1.18	1.02
0.40	9.75	57.84	0.00	8.20	1.96	1.67
0.55	6.94	70.00	0.00	9.60	2.64	2.36
0.66	4.69	76.22	0.00	11.60	3.27	2.95
0.80	4.75	79.46	0.00	13.21	3.66	3.46

Tab. I - A. Benoni et al., “Towards Real-World Indoor Smart ...”

<i>Hallway</i>	<i>Area</i>	<i>RoI Area</i>	<i>EMS Side</i>	<i>RoI Area</i>	<i>RoI Reduction</i>	ΔP_{RX}^{\min}	ΔP_{RX}^{\max}	$\Delta P_{RX}^{\text{avg}}$	$\Delta P_{RX}^{\text{dev}}$
γ	[m ²]	$\Lambda_{Ref}(\Omega)$ [m ²]	L [m]	$\Lambda_{SEME}(\Omega)$ [m ²]	$\rho(\Omega)$ [%]	[dB]	[dB]	[dB]	[dB]
<i>B</i>	67.5	21.88	0.55	6.06	72.29	0.00	8.21	2.52	1.78
<i>C</i>	60.0	0.8	0.32	0.00	100	0.00	3.87	0.84	0.51
<i>D</i>	40.5	-	-	-	-	-	-	-	-
<i>E</i>	40.5	-	-	-	-	-	-	-	-

Tab. II - A. Benoni et al., "Towards Real-World Indoor Smart ..."

	<i>Reference</i>				<i>SEME</i>				Ξ
	min	max	avg	std	min	max	avg	std	
\mathcal{D} [Mbps]	74.94	110.12	95.79	8.87	109.60	131.16	127.98	5.91	33.6 %
$\mathcal{L}_{\mathcal{D}}$ [msec]	18.00	189.00	122.87	50.92	16.00	73.00	52.13	15.99	-57.6 %
\mathcal{U} [Mbps]	77.14	84.49	81.57	2.62	80.54	108.19	97.18	9.79	19.1 %
$\mathcal{L}_{\mathcal{U}}$ [msec]	24.00	116.00	43.33	23.58	11.00	25.00	20.40	4.00	-52.9 %

Tab. III - A. Benoni et al., “Towards Real-World Indoor Smart ...”

	$\Delta Cost$ (w.r.t. Reference)		
	Reference (AP)	SEME (AP & SP-EMS)	Standard (2 APs)
<i>Device Purchase</i> (C_a) [\$]	0	100	700
<i>Device Installation</i> (C_c) [\$]	0	5	300
<i>Energy Cost</i> (C_o) [\$/year]	0	0	50
<i>Device Removal</i> (C_d) [\$]	0	0	100
<i>TCO</i> (C)	0 [\$] + 0 [\$/year]	105 [\$] + 0 [\$/year]	1100 [\$] + 50 [\$/year]
<i>5-Years TCO</i> [\$]	0	105	1350

Tab. IV - A. Benoni et al., “Towards Real-World Indoor Smart ...”